Planck 2013 results. XX. Cosmology from Sunyaev–Zeldovich cluster counts

Planck Collaboration: P. A. R. Ade[95], N. Aghanim[66], C. Armitage-Caplan[101], M. Arnaud[79], M. Ashdown[76,7], F. Atrio-Barandela[21], J. Aumont[66], C. Baccigalupi[93], A. J. Banday[105,11], R. B. Barreiro[73], R. Barrena[72], J. G. Bartlett[1,74], E. Battaner[107], R. Battye[75], K. Benabed[67,104], A. Benoît[64], A. Benoit-Lévy[29,67,104], J.-P. Bernard[11], M. Bersanelli[40,56], P. Bielewicz[105,11,93], I. Bikmaev[24,3], A. Blanchard[105], J. Bobin[79], J. J. Bock[74,12], H. Böhringer[85], A. Bonaldi[75], J. R. Bond[10], J. Borrill[16,98], F. R. Bouchet[67,104], H. Bourdin[42], M. Bridges[76,7,70], M. L. Brown[75], M. Bucher[1], R. Burenin[97,88], C. Burigana[55,38], R. C. Butler[55], J.-F. Cardoso[80,1,67], P. Carvalho[7], A. Catalano[81,78], A. Challinor[70,76,13], A. Chamballu[79,18,66], R.-R. Chary[63], L.-Y Chiang[69], H. C. Chiang[32,8], G. Chon[85], P. R. Christensen[89,43], S. Church[100], D. L. Clements[62], S. Colombi[67,104], L. P. L. Colombo[28,74], F. Couchot[77], A. Coulais[78], B. P. Crill[74,90], A. Curto[7,73], F. Cuttaia[55], A. Da Silva[14], H. Dahle[71], L. Danese[93], R. D. Davies[75], R. J. Davis[75], P. de Bernardis[39], A. de Rosa[55], G. de Zotti[52,93], J. Delabrouille[1], J.-M. Delouis[67,104], J. Démoclès[79], F.-X. Désert[59], C. Dickinson[75], J. M. Diego[73], K. Dolag[106,84], H. Dole[66,65], S. Donzelli[56], O. Doré[74,12], M. Douspis[66∗], X. Dupac[46], G. Efstathiou[70], T. A. Enßlin[84], H. K. Eriksen[71], F. Finelli[55,57], I. Flores-Cacho[11,105], O. Forni[105,11], M. Frailis[54], E. Franceschi[55], S. Fromenteau[1,66], S. Galeotta[54], K. Ganga[1], R. T. Génova-Santos[72], M. Giard[105,11], G. Giardino[47], Y. Giraud-Héraud[1], J. González-Nuevo[73,93], K. M. Górski[74,109], S. Gratton[76,70], A. Gregorio[41,54], A. Gruppuso[55], F. K. Hansen[71], D. Hanson[86,74,10], D. Harrison[70,76], S. Henrot-Versillé[77], C. Hernández-Monteagudo[15,84], D. Herranz[73], S. R. Hildebrandt[12], E. Hivon[67,104], M. Hobson[7], W. A. Holmes[74], A. Hornstrup[19], W. Hovest[84], K. M. Huffenberger[108], G. Hurier[66,81], T. R. Jaffe[105,11], A. H. Jaffe[62], W. C. Jones[32], M. Juvela[31], E. Keihänen[31], R. Keskitalo[26,16], I. Khamitov[102,24], T. S. Kisner[83], R. Kneissl[45,9], J. Knoche[84], L. Knox[34], M. Kunz[20,66,4], H. Kurki-Suonio[31,50], G. Lagache[66], A. Lähteenmäki[2,50], J.-M. Lamarre[78], A. Lasenby[7,76], R. J. Laureijs[47], C. R. Lawrence[74], J. P. Leahy[75], R. Leonardi[46], J. León-Tavares[48,2], J. Lesgourgues[103,92], A. Liddle[94,30], M. Liguori[37], P. B. Lilje[71], M. Linden-Vørnle[19], M. López-Caniego[73], P. M. Lubin[35], J. F. Macías-Pérez[81], B. Maffei[75], D. Maino[40,56], N. Mandolesi[55,6,38], A. Marcos-Caballero[73], M. Maris[54], D. J. Marshall[79], P. G. Martin[10], E. Martínez-González[73], S. Masi[39], S. Matarrese[37], F. Matthai[84], P. Mazzotta[42], P. R. Meinhold[35], A. Melchiorri[39,58], J.-B. Melin[18], L. Mendes[46], A. Mennella[40,56], M. Migliaccio[70,76], S. Mitra[61,74], M.-A. Miville-Deschênes[66,10], A. Moneti[67], L. Montier[105,11], G. Morgante[55], D. Mortlock[62], A. Moss[96], D. Munshi[95], P. Naselsky[89,43], F. Nati[39], P. Natoli[38,5,55], C. B. Netterfield[23], H. U. Nørgaard-Nielsen[19], F. Noviello[75], D. Novikov[62], I. Novikov[89], S. Osborne[100], C. A. Oxborrow[19], F. Paci[93], L. Pagano[39,58], F. Pajot[66], D. Paoletti[55,57], B. Partridge[49], F. Pasian[54], G. Patanchon[1], O. Perdereau[77], L. Perotto[81], F. Perrotta[93], F. Piacentini[39], M. Piat[1], E. Pierpaoli[28], D. Pietrobon[74], S. Plaszczynski[77], E. Pointecouteau[105,11], G. Polenta[5,53], N. Ponthieu[66,59], L. Popa[68], T. Poutanen[50,31,2], G. W. Pratt[79], G. Prézeau[12,74], S. Prunet[67,104], J.-L. Puget[66], J. P. Rachen[25,84], R. Rebolo[72,17,44], M. Reinecke[84], M. Remazeilles[66,1], C. Renault[81], S. Ricciardi[55], T. Riller[84], I. Ristorcelli[105,11], G. Rocha[74,12], M. Roman[1], C. Rosset[1], G. Roudier[1,78,74], M. Rowan-Robinson[62], J. A. Rubiño-Martín[72,44], B. Rusholme[63], M. Sandri[55], D. Santos[81], G. Savini[91], D. Scott[27], M. D. Seiffert[74,12], E. P. S. Shellard[13], L. D. Spencer[95], J.-L. Starck[79], V. Stolyarov[7,76,99], R. Stompor[1], R. Sudiwala[95], R. Sunyaev[84,97], F. Sureau[79], D. Sutton[70,76], A.-S. Suur-Uski[31,50], J.-F. Sygnet[67], J. A. Tauber[47], D. Tavagnacco[54,41], L. Terenzi[55], L. Toffolatti[22,73], M. Tomasi[56], M. Tristram[77], M. Tucci[20,77], J. Tuovinen[87], M. Türler[60], G. Umana[51], L. Valenziano[55], J. Valiviita[50,31,71], B. Van Tent[82], P. Vielva[73], F. Villa[55], N. Vittorio[42], L. A. Wade[74], B. D. Wandelt[67,104,36], J. Weller[106], M. White[33], S. D. M. White[84], D. Yvon[18], A. Zacchei[54], and A. Zonca[35]

(Affiliations can be found after the references)

Preprint online version: March 20, 2013

ABSTRACT

We present constraints on cosmological parameters using number counts as a function of redshift for a sub-sample of 189 galaxy clusters from the *Planck* SZ (PSZ) catalogue. The PSZ is selected through the signature of the Sunyaev–Zeldovich (SZ) effect, and the sub-sample used here has a signal-to-noise threshold of seven, with each object confirmed as a cluster and all but one with a redshift estimate. We discuss the calculation of the expected cluster counts as a function of cosmological parameters, the completeness of the sample, and the likelihood construction method. Using a relation between mass M and SZ signal Y based on comparison to X-ray measurements, we derive constraints on the power spectrum amplitude σ_8 and matter density parameter $\Omega_{\rm m}$ in a flat ΛCDM model. We test the robustness of our estimates and find that possible biases in the Y–M relation and the halo mass function appear larger than the statistical uncertainties from the cluster sample. Assuming a bias between the X-ray determined mass and the true mass of 20%, motivated by comparison of the observed mass scaling relations to those from a set of numerical simulations, we find that $\sigma_8(\Omega_{\rm m}/0.27)^{0.3} = 0.78 \pm 0.01$, with one-dimensional ranges $\sigma_8 = 0.77 \pm 0.02$ and $\Omega_{\rm m} = 0.29 \pm 0.02$. The values of the cosmological parameters are degenerate with the mass bias, and it is found that the larger values of σ_8 and $\Omega_{\rm m}$ preferred by the *Planck*'s measurements of the primary CMB anisotropies can be accommodated by a mass bias of about 45%. Alternatively, consistency with the primary CMB constraints can be achieved by inclusion of processes that suppress power on small scales, such as a component of massive neutrinos. We place our results in the context of other determinations of cosmological parameters, and discuss issues that need to be resolved in order to make progress in this field.

Key words. cosmological parameters – large-scale structure of Universe – Galaxies: clusters: general

∗ Corresponding author: M. Douspis marian.douspis@ias.u-psud.fr

1. Introduction

This paper, one of a set associated with the 2013 release of data from the *Planck*[1] mission (Planck Collaboration I 2013), describes the constraints on cosmological parameters using number counts as a function of redshift for a sample of 189 galaxy clusters.

Within the standard picture of structure formation, galaxies aggregate into clusters of galaxies at late times, forming bound structures at locations where the initial fluctuations create the deepest potential wells. The study of these galaxy clusters has played a significant role in the development of cosmology over many years (see, for example, Allen et al. 2011 and Voit 2005). Their internal dynamics (Carlberg et al. 1996) and baryon fractions (White et al. 1993) have been used to infer the matter density, and this was found to be significantly below the critical density necessary to achieve a flat universe. More recently, as samples of clusters have increased in size and variety, number counts inferred from tightly-selected surveys have been used to obtain more detailed constraints on the cosmological parameters.

The early galaxy cluster catalogues were constructed by eye from photographic plates with a "richness" (or number of galaxies) attributed to each cluster (Abell 1958; Abell et al. 1989). As time has passed, new approaches for selecting clusters have been developed, most notably using X-ray emission due to thermal Bremsstrahlung radiation from the hot gas that makes up most of the baryonic matter in the cluster. X-ray cluster surveys include the NORAS (Böhringer et al. 2000) and REFLEX (Böhringer et al. 2004) surveys, based on *ROSAT* satellite observations, which have been used as source catalogues for higher-precision observations by the *Chandra* and *XMM-Newton* satellites, and surveys with *XMM-Newton*, including the *XMM* Cluster Survey (XCS, Mehrtens et al. 2012) and the *XMM* Large Scale Structure survey (XMM-LSS, Willis et al. 2013).

To exploit clusters for cosmology, a key issue is how the properties used to select and characterize the cluster are related to the total mass of the cluster, since this is the quantity most readily predicted from theoretical models. Galaxies account for a small fraction of the cluster mass and the scatter between richness and mass appears to be large. However, there are a number of other possibilities. In particular, there are strong correlations between the total mass and both the integrated X-ray surface brightness and X-ray temperature, making them excellent mass proxies.

The Sunyaev–Zeldovich (SZ) effect (Sunyaev & Zeldovich 1970; Zeldovich & Sunyaev 1969) is the inverse Compton scattering of cosmic microwave background (CMB) photons by the hot gas along the line of sight, and this is most significant when the line of sight passes through a galaxy cluster. It leads to a decrease in the overall brightness temperature in the Rayleigh–Jeans portion of the spectrum and an increase in the Wien tail, with a null around 217 GHz (see Birkinshaw 1999 for a review). The amplitude of the SZ effect is given by the integrated pressure of the gas within the cluster along the line of sight. Evidence both from observation (Marrone et al. 2012; Planck Collaboration Int. III 2013) and from numerical simulations (Springel et al. 2001; da Silva et al. 2004; Motl et al. 2005; Nagai 2006a; Kay et al. 2012a) suggests that this is an excellent mass proxy. A number of articles have discussed the possibility of using SZ-selected cluster samples to constrain cosmological parameters (Barbosa et al. 1996; Aghanim et al. 1997; Haiman et al. 2001; Holder et al. 2001; Weller et al. 2002; Diego et al. 2002; Battye & Weller 2003).

This paper describes the constraints on cosmological parameters imposed by a high signal-to-noise (S/N) sub-sample of the *Planck* SZ Catalogue (PSZ, see Planck Collaboration XXIX 2013, henceforth Paper 1, for details of the entire catalogue) of nearly 200 clusters (shown in Fig. 1). This sub-sample has been selected to be pure, in the sense that all the objects within it have been confirmed as clusters via additional observations, either from the literature or undertaken by the *Planck* collaboration. In addition all objects but one have an identified redshift, either photometric or spectroscopic. This is the largest SZ-selected sample of clusters used to date for this purpose. We will show that it is the systematic uncertainties from our imperfect knowledge of cluster properties that dominate the overall uncertainty.

The *Planck* cluster sample is complementary to those from observations using the South Pole Telescope (SPT, Carlstrom et al. 2011) and the Atacama Cosmology Telescope (ACT, Swetz et al. 2011), whose teams recently published the first large samples of SZ-selected clusters (Reichardt et al. 2012a; Hasselfield et al. 2013). The resolution of *Planck* at the relevant frequencies is between 5 and 10 arcmin, whereas that for ACT and SPT it is about 1 arcmin, but the *Planck* sky coverage is much greater. This means that *Planck* typically finds larger and lower-redshift clusters than those found by SPT and ACT.

Our strategy in this first analysis is to focus on number counts of clusters, as a function of redshift, above a high S/N threshold of seven and to explore the robustness of the results. We do not use the observed SZ brightness of the clusters, due to the significant uncertainty caused by the size–flux degeneracy, as discussed in Paper 1. Accordingly, our theoretical modelling of the cluster population is directed at determining the expected number of clusters in each redshift bin exceeding the S/N threshold, and again does not otherwise use the predicted cluster SZ signal. The predicted and observed numbers of clusters are then compared in order to obtain the likelihood. In the future, we will make use of the SZ-estimated mass and a larger cluster sample to extend the analysis to broader cosmological scenarios.

This paper is laid out as follows. We describe the theoretical modelling of the redshift number counts in Sect. 2, while Sect. 3 presents the *Planck* SZ cosmological sample and selection function used in this work. The likelihood we adopt for putting constraints on cosmological parameters in given in Sect. 4. Section 5 presents our results on cosmological parameter estimation and the robustness of our results. We discuss how they fit in with other cluster and cosmological constraints in Sect. 6, before providing a final summary. A detailed discussion of our calibration of the SZ flux versus mass relation and its uncertainties is given in Appendix A.

2. Modelling cluster number counts

2.1. Model definitions

We parameterize the standard cosmological model as follows. The densities of various components are specified relative to the present-day critical density, with $\Omega_X = \rho_X/\rho_{crit}$ denoting that for component X. These components always include matter, Ω_m, and a cosmological constant Ω_Λ. For this work we assume that the Universe is flat, that is, $\Omega_m + \Omega_\Lambda = 1$ and the optical depth to reionization if fixed, $\tau = 0.085$, except in the CMB+SZ analyses.

[1] *Planck* (http://www.esa.int/Planck) is a project of the European Space Agency (ESA) with instruments provided by two scientific consortia funded by ESA member states (in particular the lead countries France and Italy), with contributions from NASA (USA) and telescope reflectors provided by a collaboration between ESA and a scientific consortium led and funded by Denmark.

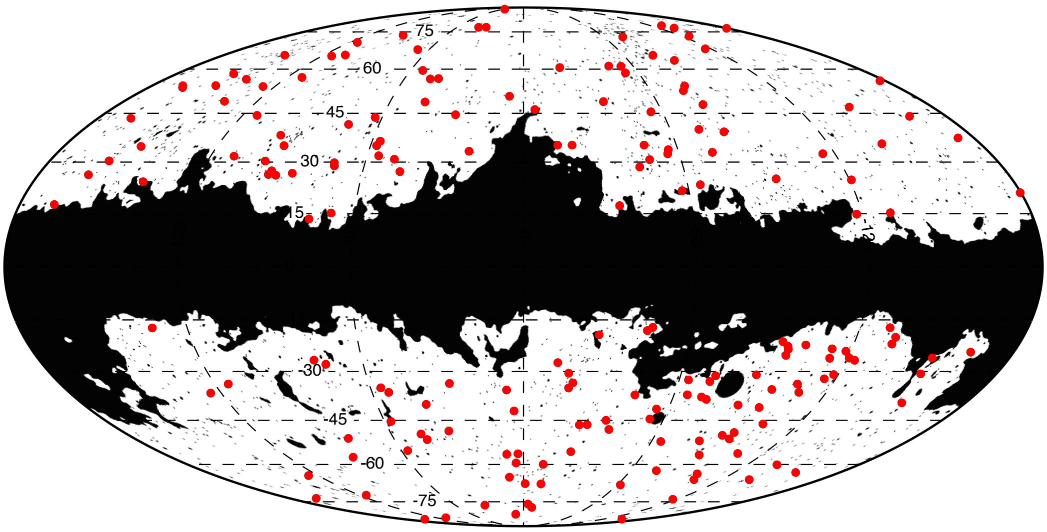

Fig. 1. The distribution on the sky of the *Planck* SZ cluster sub-sample used in this paper, with the 35% mask overlaid.

The present-day expansion rate of the Universe is quantified by the Hubble constant $H_0 = 100\,h\,\mathrm{km\,s^{-1}\,Mpc^{-1}}$.

The cluster number counts are very sensitive to the amplitude of the matter power spectrum. When studying cluster counts it is usual to parametrize this in terms of the density variance in spheres of radius $8h^{-1}$ Mpc, denoted σ_8, rather than overall power spectrum amplitude, A_s. In cases where we include primary CMB data we use A_s and compute σ_8 as a derived parameter. In addition to the parameters above, we also allow the other standard cosmological parameters to vary: n_s representing the spectral index of density fluctuations; and $\Omega_b h^2$ quantifying the baryon density.

The number of clusters predicted to be observed by a survey in a given redshift interval $[z_i, z_{i+1}]$ can be written

$$n_i = \int_{z_i}^{z_{i+1}} dz \frac{dN}{dz} \quad (1)$$

with

$$\frac{dN}{dz} = \int d\Omega \int dM_{500}\, \hat{\chi}(z, M_{500}, l, b)\, \frac{dN}{dz\, dM_{500}\, d\Omega}\,, \quad (2)$$

where $d\Omega$ is the solid angle element and M_{500} is the mass within the radius where the mean enclosed density is 500 times the critical density. The quantity $\hat{\chi}(z, M_{500}, l, b)$ is the survey completeness at a given location (l, b) on the sky, given by

$$\hat{\chi} = \int dY_{500} \int d\theta_{500} P(z, M_{500}|Y_{500}, \theta_{500})\, \chi(Y_{500}, \theta_{500}, l, b)\,. \quad (3)$$

Here $P(z, M_{500}|Y_{500}, \theta_{500})$ is the distribution of (z, M_{500}) for a given (Y_{500}, θ_{500}), where Y_{500} and θ_{500} are the SZ flux and size of a cluster of redshift and mass (z, M_{500}).

This distribution is obtained from the scaling relations between Y_{500}, θ_{500}, and M_{500}, discussed later in this section. Note that $\hat{\chi}(z, M_{500}, l, b)$ depends on cosmological parameters through $P(z, M_{500}|Y_{500}, \theta_{500})$, while the completeness in terms of the observables, $\chi(Y_{500}, \theta_{500}, l, b)$, does not depend on the cosmology as it refers directly to the observed quantities.

For the present work, we restrict our analysis to the quantity dN/dz which measures the total counts in redshift bins. In particular, we do not use the blind SZ flux estimated by the cluster candidate extraction methods that, as detailed in Planck Collaboration VIII (2011), is found to be significantly higher than the flux predicted from X-ray measurements. In contrast to the blind SZ flux, the blind S/N is in good agreement with the S/N measured using X-ray priors. Figure 2 shows the blind S/N ($\mathrm{S/N_{blind}}$) versus the S/N re-extracted at the X-ray position and using the X-ray size ($\mathrm{S/N_X}$). The clusters follow the equality line. In Sect. 3, we use the ($\mathrm{S/N_{blind}}$) values to define our cosmological sample, while for the predicted counts (defined in Sect. 2) we use the completeness based on $\mathrm{S/N_X}$. Our analysis relies on the good match between these two quantities.

To carry out a prediction of the counts expected in a survey, given cosmological assumptions, we therefore need the following inputs:

- a mass function that tells us the number distribution of clusters with mass and redshift;
- scaling relations that can predict observable quantities from the mass and redshift;
- the completeness of the survey in terms of those observables, which tells us the probability that a model cluster would make it into the survey catalogue.

These are described in the remainder of this section and in the next.

2.2. Mass function

Our main results use the mass function from Tinker et al. (2008), which is given by

$$\frac{dN}{dM_{500}}(M_{500}, z) = f(\sigma)\, \frac{\rho_m(z=0)}{M_{500}}\, \frac{d\ln\sigma^{-1}}{dM_{500}}\,, \quad (4)$$

where

$$f(\sigma) = A\left[1 + \left(\frac{\sigma}{b}\right)^{-a}\right] \exp\left(-\frac{c}{\sigma^2}\right), \quad (5)$$

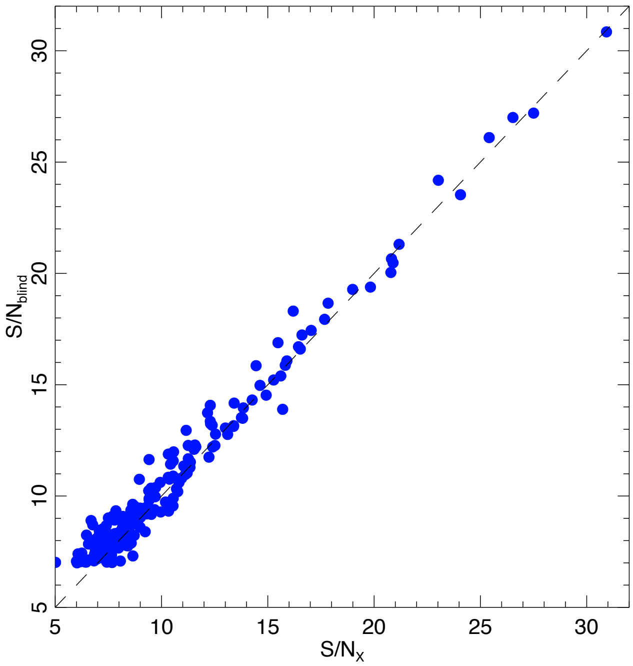

Fig. 2. Blind S/N versus S/N re-extracted at the X-ray position using the X-ray size, for the `MMF3` detections of *Planck* clusters that are associated with known X-ray clusters in the reference cosmological sample. In contrast to the blind SZ flux, the blind S/N is in good agreement with S/N measured using X-ray priors.

and $\rho_{\rm m}(z = 0)$ is the mean matter density at $z = 0$. The coefficients A, a, b and c are tabulated in Tinker et al. (2008) for different overdensities, $\Delta_{\rm mean}$, with respect to the mean cosmic density, and depend on z. Here we use $\Delta_{\rm critical} = 500$ relative to the critical density, so we compute the relevant mass function coefficients by interpolating the Tinker et al. (2008) tables for halos with $\Delta_{\rm mean} \equiv \Delta_{\rm critical}/\Omega_{\rm m}(z) = 500/\Omega_{\rm m}(z)$, where $\Omega_{\rm m}(z)$ is the matter density parameter at redshift z.

The quantity σ is the standard deviation, computed in linear perturbation theory, of the density perturbations in a sphere of radius R, which is related to the mass by $M = 4\pi\rho_{\rm m}(z = 0)R^3/3$. It is given by

$$\sigma^2 = \frac{1}{2\pi^2}\int dk\, k^2 P(k,z)|W(kR)|^2\,, \tag{6}$$

where $P(k, z)$ is the matter power spectrum at redshift z, which we compute for any given set of cosmological parameters using `CAMB` (Lewis et al. 2000), and $W(x) = 3(\sin x - x\cos x)/x^3$ is the filter function of a spherical top hat of radius R.

The quantity $dN/(dz\, dM_{500}\, d\Omega)$ in Eq. 2 is computed by multiplying the mass function $dN(M_{500}, z)/dM_{500}$ by the volume element $dV/(dz\, d\Omega)$.

As a baseline we use, except where stated otherwise, the Tinker et al. (2008) mass function, but we consider an alternative mass function as a cross-check. In a recent publication by Watson et al. (2012), a new mass function is extracted from the combination of large cosmological simulations (typical particle numbers of 3000^3 to 6000^3) with a very large dynamic range (size from $11\,h^{-1}$ to $6000\,h^{-1}$Mpc), which extends the maximum volume probed by Tinker et al. by two orders of magnitude. The two mass functions agree fairly well, except in the case of the most massive objects, where Tinker et al.'s mass function predicts more clusters than Watson et al.'s. The Tinker et al. mass function might be derived from volumes that are not large enough to properly sample the rarer clusters. These rare clusters are more relevant for *Planck* than for ground-based SZ experiments, which probe smaller areas of the sky. The Watson et al. mass function is used only in Sect. 5.3, which deals with mass function uncertainties.

Table 1. Summary of scaling-law parameters and error budget. Note that β is kept fixed at its central value except in Sect. 5.3.

$\log Y_*$	-0.19 ± 0.02
α	1.79 ± 0.08
β	0.66 ± 0.50
$\sigma_{\log Y}$	0.075 ± 0.01

2.3. Scaling relations

A key issue is to relate the observed SZ flux, Y_{500}, to the mass M_{500} of the cluster. As we show in Sect. 5, cosmological constraints are sensitive to the normalization and slope of the assumed Y_{500}–M_{500} relation. We thus paid considerable attention to deriving the most accurate scaling relations possible, with careful handling of statistical and systematic uncertainties, and to testing their impact on the derived cosmological parameters.

The baseline relation is obtained from an observational calibration of the Y_{500}–M_{500} relation on one-third of the cosmological sample, using the mass derived from the X-ray $Y_{\rm X}$–M_{500} relation, $M_{500}^{Y_{\rm X}}$, as a mass proxy. Here $Y_{\rm X}$ is the X-ray analogue of the SZ signal, defined in Appendix A. Y_{500} is then measured interior to $R_{500}^{Y_{\rm X}}$, the radius corresponding to $M_{500}^{Y_{\rm X}}$. The relation is corrected for Malmquist bias effects, and we carefully propagate the statistical and systematic uncertainties on the relation between $M_{500}^{Y_{\rm X}}$ and the true mass M_{500}. The mean bias between these two quantities, $(1-b)$, has been estimated from comparison with the predictions from several sets of numerical simulations, as detailed in Appendix A.

The large uncertainties on $(1 - b)$ are due to the dispersion in predictions from the various simulation sets, which is a limiting factor in our analysis. In the following, our baseline approach is to fix b to the value $(1 - b) = 0.80$. This value is to be considered an average over the cluster population, and is assumed to be redshift independent. On a cluster-by-cluster basis it would be expected to be stochastic, contributing to scatter in the Y_{500}–M_{500} relation given below. In our analysis of systematic uncertainties on the derived cosmological parameters, we also consider a case where $(1 - b)$ can vary occupying the range $[0.7, 1.0]$ with a flat prior.

As detailed in Appendix A, we derive a baseline relation for the mean SZ signal $\bar{Y}_{500}$ from a cluster of given mass and redshift in the form

$$E^{-\beta}(z)\left[\frac{D_{\rm A}^2(z)\,\bar{Y}_{500}}{10^{-4}\,{\rm Mpc}^2}\right] = Y_*\left[\frac{h}{0.7}\right]^{-2+\alpha}\left[\frac{(1-b)\,M_{500}}{6\times10^{14}\,{\rm M_{sol}}}\right]^{\alpha}, \tag{7}$$

where $D_{\rm A}(z)$ is the angular-diameter distance to redshift z and $E^2(z) = \Omega_{\rm m}(1 + z)^3 + \Omega_\Lambda$. The coefficients Y_*, α and β are given in Table 1.

Equation 7 has an estimated intrinsic scatter[2] $\sigma_{\log Y} = 0.075$, which we take to be independent of redshift (see Appendix A).

[2] Throughout this article, log is base 10 and ln is base e.

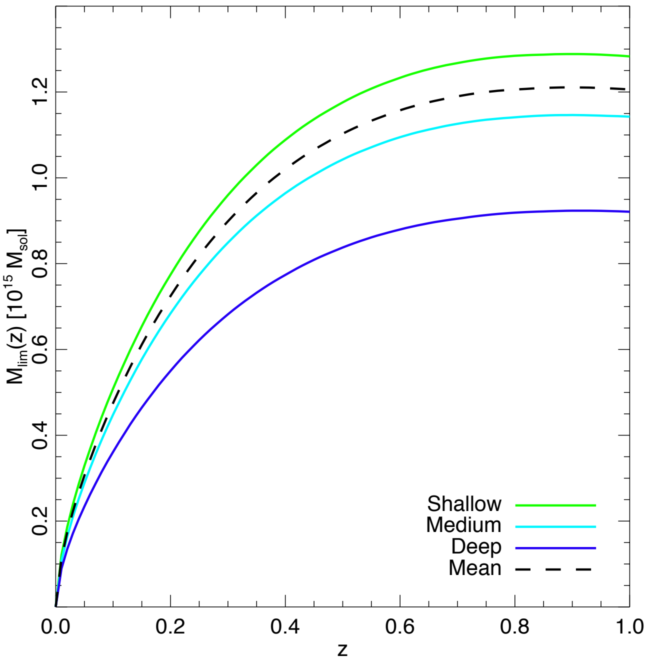

Fig. 3. Limiting mass as a function of z for the selection function and noise level computed for three zones (deep, blue; medium, cyan; shallow, green), and on average for the unmasked sky (dashed black).

This is incorporated by drawing the cluster's Y_{500} from a log-normal distribution

$$\mathcal{P}(\log Y_{500}) = \frac{1}{\sqrt{2\pi\sigma^2_{\log Y}}} \exp\left[-\frac{\log^2(Y_{500}/\bar{Y}_{500})}{2\sigma^2_{\log Y}}\right], \quad (8)$$

where $\bar{Y}_{500}$ is given by Eq. 7. Inclusion of this scatter increases the number of clusters expected at a given S/N; since the cluster counts are a steep function of M_{500} in the range of mass in question, there are more clusters that scatter upwards from below the limit given by the zero-scatter scaling relation than those that scatter downwards.

In addition to Eq. 7 we need a relation between θ_{500} (in fact $\theta_{500}^{Y_X}$, the angular size corresponding to the physical size $R_{500}^{Y_X}$), the aperture used to extract Y_{500}, and M_{500}. Since $M_{500} = 500 \times 4\pi\rho_{\rm crit}R^3_{500}/3$ and $\theta_{500} = R_{500}/D_{\rm A}$, this can be expressed as

$$\bar{\theta}_{500} = \theta_* \left[\frac{h}{0.7}\right]^{-2/3} \left[\frac{(1-b)\,M_{500}}{3\times10^{14}{\rm M_{sol}}}\right]^{1/3} E^{-2/3}(z) \left[\frac{D_{\rm A}(z)}{500\,{\rm Mpc}}\right]^{-1}, \quad (9)$$

where $\theta_* = 6.997$ arcmin.

2.4. Limiting mass

One can use Eqs. 7 and 9 to compute the limiting mass at a point on the sky where the noise level, σ_Y, has been computed as described in Sect. 3. As the latter is not homogeneous on the sky, we show in Fig. 3 the limiting mass, defined at 50% completeness, as a function of redshift for three different zone, deep, medium, and shallow, covering respectively, 3.5%, 48.8% and 48.7% of the unmasked sky. For each line a S/N cut of 7 has been adopted.

2.5. Implementation

We have implemented three independent versions of the computation of counts and constraints. The differences in predicted counts are of the order of a few percent, which translates to less than a tenth of 1 σ on the cosmological parameters of interest.

3. The *Planck* cosmological samples

3.1. Sample definition

The reference cosmological sample is constructed from the *Planck* SZ Catalogue (PSZ) published in Planck Collaboration XXIX (2013) and made public with the first release of *Planck* cosmological products. It is based on the SZ detections performed with the Matched Multi-filter (MMF) method MMF3 (Melin et al. 2006), which relies on use of a filter of adjustable width θ_{500} chosen to maximize the S/N of the detection. In order to ensure a high purity and to maximize the number of redshifts, the cosmological sample was constructed by selecting the SZ detections above a S/N threshold of 7 outside Galactic and point source masks covering 35% of the sky, as discussed in Paper 1. From the original PSZ, only the information on S/N (for the selection) and redshift are used.

This sample contains 189 candidates. All but one are confirmed bona fide clusters with measured redshifts, including 184 spectroscopic redshifts. Among these confirmed clusters 12 were confirmed with follow-up programmes conducted by the *Planck* collaboration (see Paper 1 for details). The remaining non-confirmed cluster candidate is a high-reliability CLASS1 candidate, meaning that its characterization as a cluster is supported by data in other wavebands (see Paper 1 for details). It is thus considered as a bona fide cluster. The distribution on the sky of this baseline cosmological sample is shown in Fig. 1.

In addition to our reference sample, we consider two other samples drawn from the PSZ for consistency checks. One is based on the detections from the second implementation of the MMF algorithm, MMF1, described in Paper 1. It contains 188 clusters with S/N > 7 and no missing redshifts, with almost complete overlap with the baseline sample (187 clusters in common). The third sample considered in the present study is also based on MMF3 detections but with a higher S/N cut of S/N > 8. It allows us to test selection effects and to probe the consistency of the results as a function of the S/N cut. It contains 136 clusters, all with measured redshifts.

The selection function for each of these samples is constructed as described in the next section.

3.2. Completeness

The completeness of the reference cosmological sample is computed with two distinct and complementary approaches: a semi-analytic approach based on the assumption of Gaussian uncertainties; and a computational approach based on Monte Carlo cluster injection into real sky maps.

The completeness χ can be evaluated analytically by setting the probability of the measured SZ flux, Y_{500}, to be Gaussian distributed with a standard deviation equal to the noise, $\sigma_{Y_{500}}(\theta_{500}, l, b)$, computed for each size θ_{500} of the MMF filter and at each position (l, b) on the sky:

$$\chi_{\rm erf}(Y_{500}, \theta_{500}, l, b) = \frac{1}{2}\left[1 + {\rm erf}\left(\frac{Y_{500} - X\,\sigma_{Y_{500}}(\theta_{500}, l, b)}{\sqrt{2}\,\sigma_{Y_{500}}(\theta_{500}, l, b)}\right)\right], \quad (10)$$

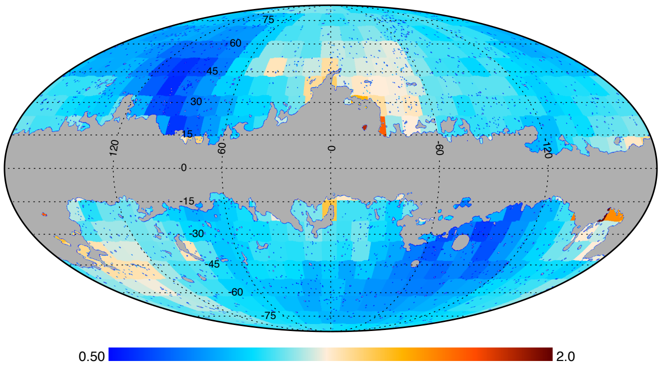

Fig. 4. Noise map $\sigma_{Y_{500}}(\theta_{500})$ for $\theta_{500} = 6$ arcmin. The PSZ is limited by instrumental noise at high ($|b| > 20°$) Galactic latitude (deeper at ecliptic poles) and foreground noise at low Galactic latitude. The scale of the map ranges from 0.5 to 2 times the mean noise of the map, which is $\langle\sigma_{Y_{500}}(6 \text{ arcmin})\rangle = 2.2 \times 10^{-4} \text{arcmin}^2$.

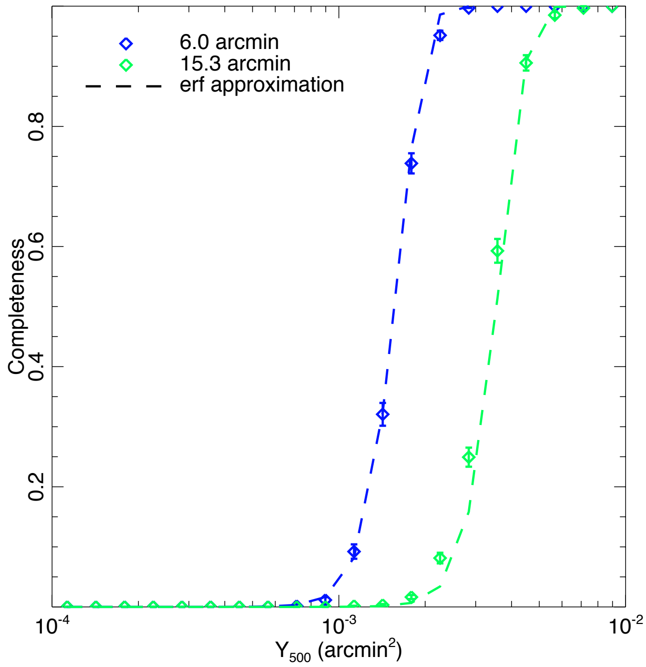

Fig. 5. Completeness averaged over the unmasked sky as a function of Y_{500} for two different filter sizes, $\theta_{500} = 6$ and 15.3 arcmin. The dashed lines show the semi-analytic approximation of Eq. 10.

where $X = 7$ is the S/N threshold and the error function is defined as usual by

$$\text{erf}(u) = \frac{2}{\sqrt{\pi}} \int_0^u \exp\left(-t^2\right) dt \,. \tag{11}$$

$\chi_{\text{erf}}(Y_{500}, \theta_{500}, l, b)$ thus lies in the range [0, 1] and gives the probability for a cluster of flux Y_{500} and size θ_{500} at position (l, b) to be detected at S/N $\geq X$.

The noise estimate $\sigma_{Y_{500}}(\theta_{500}, l, b)$ is a by-product of the detection algorithm and can be written in the form (see e.g., Melin et al. 2006)

$$\sigma_{Y_{500}}(\theta_{500}, l, b) = \left[\int d^2k \, \boldsymbol{F}^t_{\theta_{500}}(\boldsymbol{k}) \cdot \boldsymbol{P}^{-1}(\boldsymbol{k}, l, b) \cdot \boldsymbol{F}_{\theta_{500}}(\boldsymbol{k})\right]^{-1/2}, \tag{12}$$

with $\boldsymbol{F}_{\theta_{500}}(\boldsymbol{k})$ being a vector of dimension N_{freq} (the six highest *Planck* frequencies here) containing the beam-convolved cluster template scaled to the known SZ frequency dependence. The cluster template assumed is the non–standard universal pressure profile from Arnaud et al. (2010a). $\boldsymbol{P}(\boldsymbol{k}, l, b)$ is the noise power spectrum (dimension $N_{\text{freq}} \times N_{\text{freq}}$) directly estimated from the data at position (l, b). Figure 4 shows $\sigma_{Y_{500}}(\theta_{500}, l, b)$ for $\theta_{500} = 6$ arcmin in a Mollweide projection with the Galactic mask used in the analysis applied. As expected, the noise at high Galactic latitude is lower than in the areas contaminated by diffuse Galactic emission. The ecliptic pole regions have the lowest noise level, reflecting the longer *Planck* integration time in these high-redundancy areas.

The Monte Carlo (MC) completeness is calculated by injecting simulated clusters into real sky maps following the method presented in Paper 1, with the modifications that the 65% Galactic dust mask and a S/N > 7 threshold are applied to match the cosmological sample definition. The Monte Carlo completeness encodes effects not probed by the erf approximation, including the variation of cluster pressure profiles around the fiducial pressure profile used in the MMF, spatially-varying and asymmetric effective beams, and the effects of correlated non-Gaussian uncertainties in the estimation of (Y_{500}, θ_{500}). As shown in Fig. 5, the erf-based formula for the completeness is a good approximation to the Monte Carlo completeness. The agreement is best for the typical sizes probed by *Planck* (5 to 10 arcmin), though the two determinations of the completeness start to deviate for small and large sizes, due to beam and profile effects, respectively. For simplicity, we chose the erf formulation as the baseline. The effect of using the Monte Carlo completeness instead is discussed in Sect. 5.2.

4. Likelihood and Markov chain Monte Carlo

4.1. The likelihood

We now have all the information needed to predict the counts in redshift bins for our theoretical models. To obtain cosmological constraints with the *Planck* SZ sample presented in Sect. 3, we construct a likelihood function based on Poisson statistics (Cash 1979):

$$\ln L = \ln \mathcal{P}(N_i|n_i) = \sum_{i=1}^{N_b} [N_i \ln(n_i) - n_i - \ln(N_i!)] \,, \tag{13}$$

where $\mathcal{P}(N_i|n_i)$ is the probability of finding N_i clusters in each of N_b bins given an expected number of n_i in each bin in redshift. The likelihood includes bins that contain no observed clusters. As a baseline, we assume bins in redshift of $\Delta z = 0.1$ and we checked that our results are robust when changing the bin size between 0.05 and 0.2. The modelled expected number n_i depends on the bin range in redshift and on the cosmological parameters, as described in Sect. 2. It also depends on the scaling relations and the selection function of the observed sample. The parameters of the scaling relations between flux (or size) and mass and redshift are taken to be Gaussian distributed with central values and uncertainties stated in Table 1, and with the scatter in Y_{500} incorporated into the method via the log-normal distribution with width $\sigma_{\log Y}$.

In the PSZ, the redshifts have been collected from different observations and from the literature. Individual uncertainties

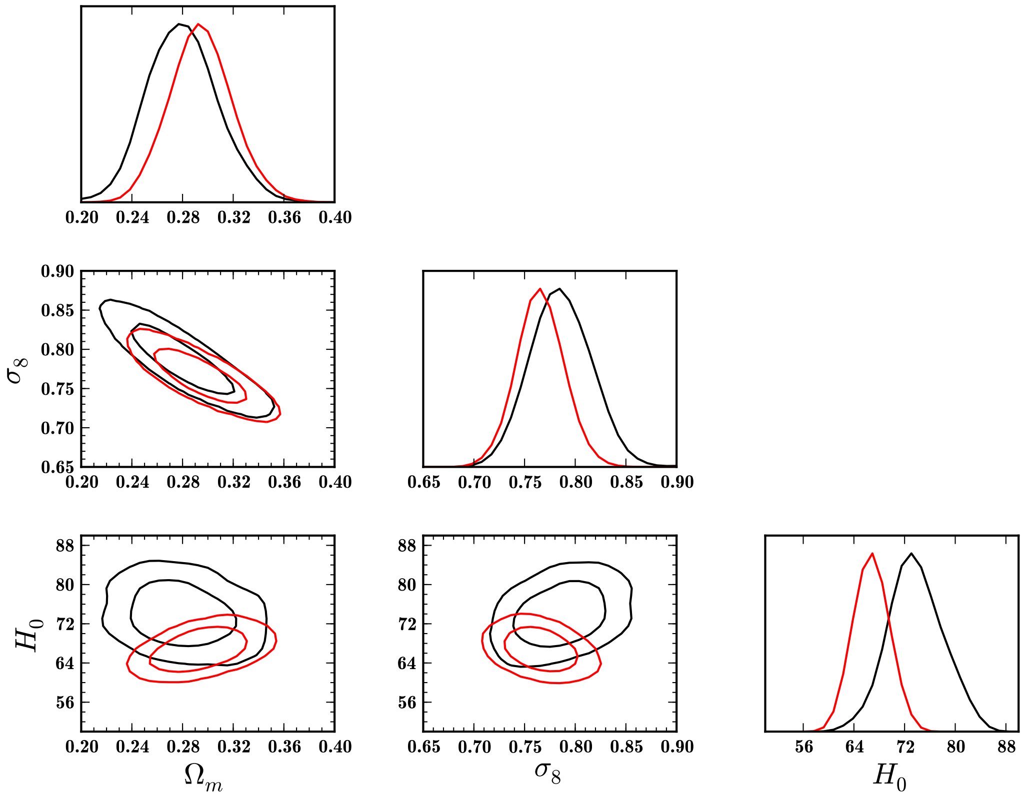

Fig. 6. *Planck* SZ constraints (+BAO+BBN) on ΛCDM cosmological parameters in red. The black lines show the constraints upon substituting the BAO constraints for H_0 constraints.

in redshift are thus spread between 0.001 and 0.1. Most of the clusters in the cosmological sample have spectroscopic redshifts (184 out of 189) and we checked that the uncertainties in redshift are not at all dominant in our error budget and are thus neglected. The cluster without known redshift is incorporated by scaling the counts by a factor 189/188, i.e., by assuming its redshift is drawn from the distribution defined by the other 188 objects.

4.2. Markov chain Monte Carlo

In order to impose constraints on cosmological parameters from our sample(s) given our modelled expected number counts, we modified `CosmoMC` (Lewis & Bridle 2002) to include the likelihood described above. We mainly study constraints on the spatially-flat ΛCDM model, varying $\Omega_{\rm m}$, σ_8, $\Omega_{\rm b}$, H_0 and $n_{\rm s}$, but also adding in the total neutrino mass, $\sum m_\nu$, in Sect. 6. In each of the runs, the nuisance parameters (Y_*, α, $\sigma_{\log Y}$) follow Gaussian priors, with the characteristics detailed in Table 1, and are marginalized over. The redshift evolution of the scaling, β, is fixed to its reference value unless stated otherwise.

4.3. External datasets

When probing the six parameters of the ΛCDM model, we combine the *Planck* clusters with the Big Bang nucleosynthesis (BBN) constraints from Steigman (2008), $\Omega_{\rm b}h^2 = 0.022 \pm 0.002$. We also use either the H_0 determination from *HST* by Riess et al. (2011), $H_0 = (73.8 \pm 2.4)$ kms^{-1}Mpc^{-1}, or baryon acoustic oscillation (BAO) data. In the latter case we adopt the combined likelihood of Hinshaw et al. (2012) and Planck Collaboration XVI (2013), which uses the radial BAO scales observed by 6dF-GRS (Beutler et al. 2011), SDSS-DR7-rec and SDSS-DR9-rec (Padmanabhan et al. 2012; Anderson et al. 2012), and WiggleZ (Blake et al. 2012).

5. Constraints from *Planck* clusters: ΛCDM

5.1. Results for $\Omega_{\rm m}$ and σ_8

Cluster counts in redshift for our *Planck* cosmological sample are not sensitive to all parameters of the ΛCDM model. We focus first on ($\Omega_{\rm m}, \sigma_8$), assuming that $n_{\rm s}$ follows a Gaussian prior centred on the best-fit *Planck* CMB value[3] ($n_{\rm s} = 0.963 \pm 0.009$). We combine our SZ counts likelihood with the BAO and BBN likelihoods discussed earlier. We also consider uncertainties on scaling parameter estimates as stated in Table 1. We furthermore assume a constant mass bias $1 - b = 0.8$.

We find the expected degeneracy between the two parameters, $\sigma_8(\Omega_{\rm m}/0.27)^{0.3} = 0.782 \pm 0.010$[4], with central values and relative uncertainties respectively of $\Omega_{\rm m} = 0.29 \pm 0.02$ and $\sigma_8 = 0.765 \pm 0.021$ (Fig. 6, red contours, and Table 2). The counts in redshift for the best-fit model are plotted in Fig. 7.

[3] Table 2 of Planck Collaboration XVI (2013).

[4] We express it this way to ease comparison with other works. The actual best fit is given by $\sigma_8(\Omega_{\rm m}/0.29)^{0.322} = 0.765 \pm 0.010$.

Table 2. Best-fit cosmological parameters for various combinations of data and analysis methods. Note that for the analysis using Watson et al. mass function, or (1-b) in [0.7-1], the degeneracy line is different and thus the value of $\sigma_8(\Omega_m/0.27)^{0.3}$ is just illustrative

	$\sigma_8(\Omega_m/0.27)^{0.3}$	Ω_m	σ_8	$1-b$
Planck SZ +BAO+BBN	0.782 ± 0.010	0.29 ± 0.02	0.77 ± 0.02	0.8
Planck SZ +HST+BBN	0.792 ± 0.012	0.28 ± 0.03	0.78 ± 0.03	0.8
`MMF1` sample +BAO+BBN	0.800 ± 0.010	0.29 ± 0.02	0.78 ± 0.02	0.8
`MMF3` S/N > 8 +BAO+BBN	0.785 ± 0.011	0.29 ± 0.02	0.77 ± 0.02	0.8
Planck SZ +BAO+BBN (MC completeness)	0.778 ± 0.010	0.30 ± 0.03	0.75 ± 0.02	0.8
Planck SZ +BAO+BBN (Watson et al. mass function)	0.802 ± 0.014	0.30 ± 0.01	0.77 ± 0.02	0.8
Planck SZ +BAO+BBN ($1-b$ in [0.7, 1.0])	0.764 ± 0.025	0.29 ± 0.02	0.75 ± 0.03	[0.7,1]

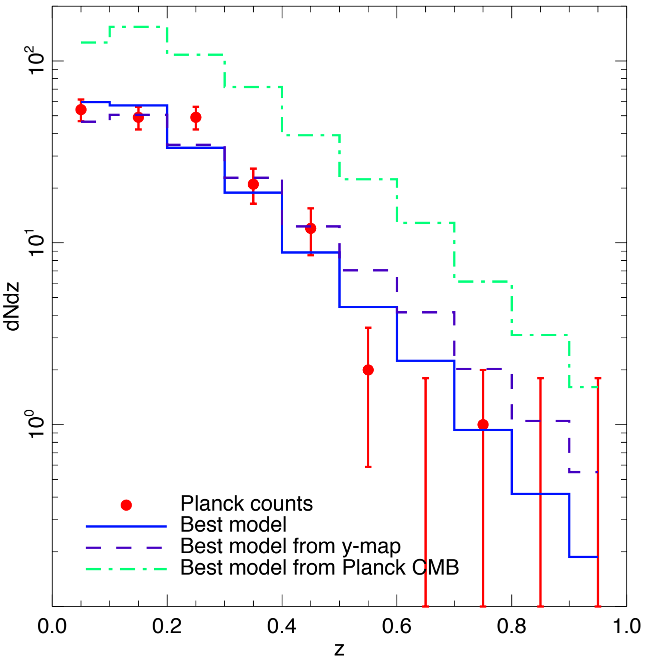

Fig. 7. Distribution in redshift for the clusters of the *Planck* cosmological sample. The observed number counts (red), are compared to our best model prediction (blue). The dashed and dot-dashed lines are the best models from the *Planck* SZ power spectrum and *Planck* CMB power spectrum fits, respectively. The uncertainties on the observed counts, shown for illustration only, are the standard deviation based on the observed counts, except for empty bins where we show the inferred 84% upper limit on the predicted counts assuming a Poissonian distribution. See Sect. 6 for more discussion.

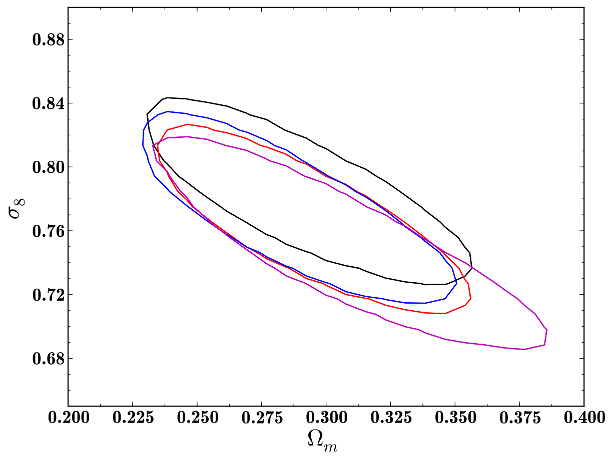

Fig. 8. 95% contours for different robustness tests: `MMF3` with S/N cut at 7 in red; `MMF3` with S/N cut at 8 in blue; and `MMF1` with S/N cut at 7 in black; and `MMF3` with S/N cut at 7 but assuming the MC completeness in purple.

To investigate how robust our results are when changing our priors, we repeat the analysis substituting the *HST* constraints on H_0 for the BAO results. Figure 6 (black contours) shows that the main effect is to change the best-fit value of H_0, leaving the (Ω_m, σ_8) degeneracy almost identical.

5.2. Robustness to observational sample

To test the robustness of our results, we performed the same analysis with different sub-samples drawn from our cosmological sample or from the PSZ, as described in Sect. 3, following that section's discussion of completeness. Figure 8 shows the likelihood contours of the three samples (blue, `MMF3` S/N > 8; red, `MMF3` S/N > 7; black, `MMF1` S/N > 7) in the (Ω_m, σ_8) plane. There is good agreement between the three samples. Obviously the three samples are not independent, as many clusters are common, but the noise estimates for `MMF3` and `MMF1` are different leading to different selection functions. Table 2 summarizes the best-fit values.

We perform the same analysis as on the baseline cosmological sample (SZ+BAO+BBN), but assuming a different computation of the completeness function using the Monte Carlo method described in Sect. 3. Figure 8 shows the change in the 2D likelihoods when the alternative approach is adopted. The Monte Carlo estimation (in purple), being close to the analytic one, gives constraints that are similar, but shifts the contour along the (Ω_m, σ_8) degeneracy.

5.3. Robustness to cluster modelling

A key ingredient in the modelling of the number counts is the mass function. Our main results adopt the Tinker et al. mass function as the reference model. We use the Watson et al. mass function to check for possible differences in our results due to the most massive/extreme clusters. Figure 9 shows the 95% contours when the different mass functions are assumed. The main effect is a change in the slope of the degeneracy between Ω_m and σ_8, moving the best-fit values by less than $1\,\sigma$.

We also relax the assumption of standard evolution of the scalings with redshift by allowing β to vary with a Gaussian prior taken from Planck Collaboration X (2011), $\beta = 0.66 \pm 0.5$. Once again, the contours move along the σ_8–Ω_m degeneracy direction (shown in blue in Fig. 9).

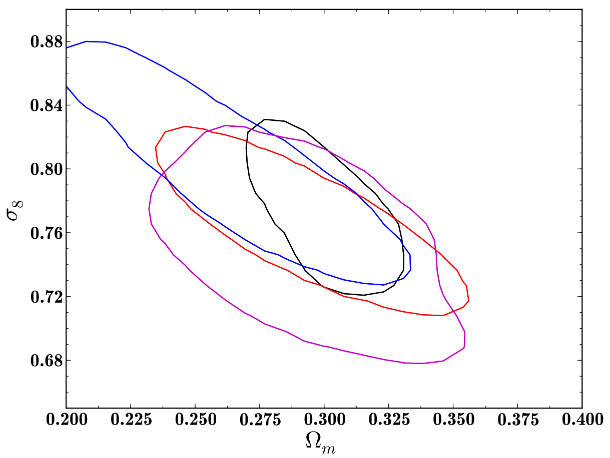

Fig. 9. Comparison of the outcome using the mass functions of Watson et al. (black) and Tinker et al. (red). Allowing the bias to vary in the range [0.7, 1.0] enlarges the constraints perpendicular to the σ_8–Ω_m degeneracy line due to the degeneracy of the number of clusters with the mass bias (purple). When relaxing the constraints on the evolution of the scaling law with redshift (blue), the contours move along the degeneracy line. Contours are 95% confidence levels here.

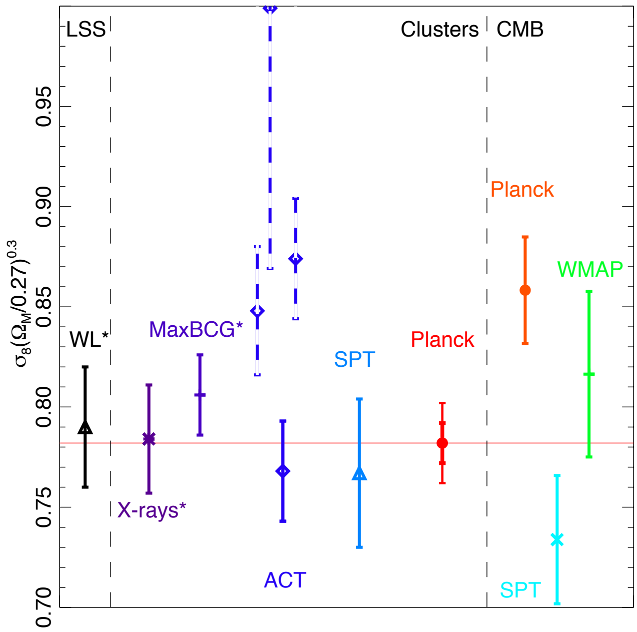

Fig. 10. Comparison of constraints (68% confidence interval) on $\sigma_8(\Omega_m/0.27)^{0.3}$ from different experiments of large–scale structure (LSS), clusters, and CMB. The solid line ACT point assumes the same universal pressure profile as this work. Probes marked with an asterisk have an original power of Ω_m different from 0.3. See text and Table 3 for more details.

As shown in Appendix A, the estimation of the mass bias is not trivial and there is a large scatter amongst simulations. We thus now allow the mass bias $(1-b)$ to vary in the range [0.7, 1.0] to reflect the uncertainty in the possible bias between the X-ray mass and the true mass for our given sample. Figure 9 shows the corresponding constraints from *Planck* SZ clusters + BAO+BBN in purple. While Ω_m is not affected much by relaxing the bias, σ_8 is now less constrained, due to the degeneracy with $(1-b)$.

6. Discussion

Our main result is the constraint in the (Ω_m, σ_8) plane for the standard ΛCDM model imposed by the SZ counts, which we have shown is robust to the details of our modelling. We now compare this result first to constraints from other cluster samples, and then to the constraints from the *Planck* analysis of the sky-map of the Compton y-parameter (Planck Collaboration XXI 2013) and of the primary CMB temperature anisotropies (Planck Collaboration XVI 2013).

6.1. Comparison with other cluster constraints

We restrict our comparison to some recent analyses exploiting a range of observational techniques to obtain cluster samples and mass calibrations.

Benson et al. (2011) used 18 galaxy clusters in the first 178 deg^2 of the SPT survey to find $\sigma_8(\Omega_m/0.25)^{0.3} = 0.785 \pm 0.037$ for a spatially-flat model. They break the degeneracy between σ_8 and Ω_m by incorporating primary CMB constraints, deducing that $\sigma_8 = 0.795 \pm 0.016$ and $\Omega_m = 0.255 \pm 0.016$. In addition, they find that the dark energy equation of state is constrained to $w = -1.09 \pm 0.36$, using just their cluster sample along with the same *HST* and BBN constraints we use. Subsequently Reichardt et al. (2012a) reported a much larger cluster sample and used this to improve on the statistical uncertainties on the cosmological parameters. Hasselfield et al. (2013) use a sample of 15 high S/N clusters from ACT, in combination with primary CMB data, to find $\sigma_8 = 0.786 \pm 0.013$ and $\Omega_m = 0.25 \pm 0.012$ when assuming a scaling law derived from the universal pressure profile.

Strong constraints on cosmological parameters have been inferred from X-ray and optical richness selected samples. Vikhlinin et al. (2009c) used a sample of 86 well-studied X-ray clusters, split into low- and high-redshift bins, to conclude that $\Omega_\Lambda > 0$ with a significance about $5\,\sigma$ and that $w = -1.14 \pm 0.21$. Rozo et al. (2010) used the approximately 10^4 clusters in the Sloan Digital Sky Survey (SDSS) MaxBCG cluster sample, which are detected using a colour–magnitude technique and characterized by optical richness. They found that $\sigma_8(\Omega_m/0.25)^{0.41} = 0.832 \pm 0.033$. Notably, the quoted uncertainty on this quantity is similar to that from the 18 clusters in the original SPT survey, even though they found over two orders of magnitude more clusters; this is because the relationship used between the optical richness and the mass has a very significant uncertainty on the scatter and absolute mass scale. In both cases much tighter constraints were found by incorporating a range of other cosmological probes.

Fig. 10 and Table 3 summarize some of the current constraints on the combination $\sigma_8(\Omega_m/0.27)^{0.3}$, which is the main degeneracy line in cluster constraints. Cosmic shear (Kilbinger et al. 2013), X-rays (Vikhlinin et al. 2009b), and MaxBCG (Rozo et al. 2010) each have a different slope in Ω_m, being 0.6, 0.47, and 0.41, respectively (instead of 0.3), as they are probing different redshift ranges. We have rescaled when necessary the best value and errors to quote numbers with a pivot $\Omega_m = 0.27$. Hasselfield et al. (2013) have derived "cluster-only" constraints from ACT by assuming several different scaling laws, shown in blue and dashed blue in Fig. 10. The constraint assuming the universal pressure profile is highlighted as

Table 3. Constraints from clusters on $\sigma_8(\Omega_m/0.27)^{0.3}$.

Experiment	CPPP[a]	MaxBCG[b]	ACT[c]	SPT	*Planck* SZ
Reference	Vikhlinin et al.	Rozo et al.	Hasselfield et al.	Reichardt et al.	This work
Number of clusters	49+37	70810	15	100	189
Redshift range	[0.025,0.25] and [0.35,0.9]	[0.1,0.3]	[0.2,1.5]	[0.3,1.35]	[0.0,0.99]
Median mass ($10^{14}h^{-1}M_{sol}$)	2.5	1.5	3.2	3.3	6.0
Probe	$N(z, M)$	$N(M)$	$N(z, M)$	$N(z, Y_X)$	$N(z)$
S/N cut	5	$(N_{200} > 11)$	5	5	7
Scaling	Y_X–T_X, M_{gas}	N_{200}–M_{200}	several	L_X–M, Y_X	Y_{SZ}–Y_X
$\sigma_8(\Omega_m/0.27)^{0.3}$	0.784 ± 0.027	0.806 ± 0.033	0.768 ± 0.025	0.767 ± 0.037	0.782 ± 0.010

[a] The degeneracy is $\sigma_8(\Omega_m/0.27)^{0.47}$.
[b] The degeneracy is $\sigma_8(\Omega_m/0.27)^{0.41}$.
[c] For ACT we choose the results assuming the universal pressure profile derived scaling law in this table (constraints with other scalings relations are shown in Fig. 10).

the solid symbol and error bar. For SPT we show the "cluster-only" constraints from Reichardt et al. (2012a). The two error bars of the *Planck* SZ cluster red point indicate the statistical and systematic ($1 - b$ free in the range $[0.7, 1.0]$) error bars. The figure thus shows good agreement amongst all cluster observations, whether in optical, X-rays, or SZ. Table 3 compares the different data and assumptions of the different cluster-related publications.

6.2. Consistency with the Planck y-map

In a companion paper (Planck Collaboration XXI 2013), we performed an analysis of the SZ angular power spectrum derived from the *Planck* y-map obtained with a dedicated component-separation technique. For the first time, the power spectrum has been measured at intermediate scales ($50 \leq \ell \leq 1000$). The same modelling as in Sect. 2 and Taburet et al. (2009, 2010) has been used to derive best-fit values of Ω_m and σ_8, assuming the universal pressure profile (Arnaud et al. 2010b), a bias $1-b = 0.8$, and the best-fit values for other cosmological parameters from Planck Collaboration XVI (2013). The best model obtained, shown in Fig. 7 as a dashed line, confirms the consistency between the *Planck* SZ number counts and the signal observed in the y-map.

6.3. Comparison with Planck primary CMB constraints

We now compare the *Planck* SZ cluster constraints to those from the analysis of the primary CMB temperature anisotropies given in Planck Collaboration XVI (2013). In that analysis σ_8 is derived from the standard six ΛCDM parameters.

The primary CMB constraints, in the (Ω_m, σ_8) plane, differ significantly from our constraints, in favouring higher values of each parameter, as seen in Fig. 11. This leads to a larger number of predicted clusters than actually observed (see Fig. 7). There is therefore some tension between the results from this analysis and our own. Figure 10 illustrates this with a comparison of three CMB analyses[5] (Planck Collaboration XVI 2013; Story et al. 2012; Hinshaw et al. 2012) with cluster constraints in terms of $\sigma_8(\Omega_m/0.27)^{0.3}$.

[5] For *Planck* CMB we derived the constraints from the chain corresponding to column 1 of Table 2 of Planck Collaboration XVI (2013). Note that the SPT results may be biased low by systematics, as discussed in the appendix of Planck Collaboration XVI (2013).

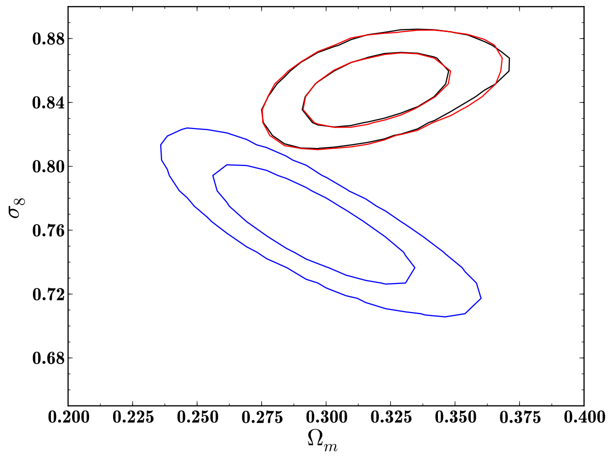

Fig. 11. 2D Ω_m–σ_8 likelihood contours for the analysis with *Planck* CMB only (red); *Planck* SZ + BAO + BBN (blue); and the combined *Planck* CMB + SZ analysis where the bias $(1 - b)$ is a free parameter (black).

It is possible that the tension results from a combination of some residual systematics with a substantial statistical fluctuation. Enough tests and comparisons have been made on the *Planck* data sets that it is plausible that at least one discrepancy at the two or three sigma level will arise by chance. Nevertheless, it is worth considering the implications of the discrepancy being real.

As we have discussed, the modelling of the cluster gas physics is the most important uncertainty in our analysis, in particular the mass bias $(1 - b)$ between the hydrostatic and true masses. While we have argued that the preferred value is $(1 - b) \simeq 0.8$, with a plausible range from 0.7 to 1, a significantly lower value would substantially alleviate the tension between CMB and SZ constraints. Performing a joint analysis using the CMB likelihood presented in Planck Collaboration XV (2013) and the cluster likelihood of this paper, we find $(1 - b) = 0.55 \pm 0.06$ and the black contours shown in Fig. 11 (in that case $(1 - b)$ was sampled in the range [0.1,1.5]). Such a large bias is difficult to reconcile with numerical simulations, and cluster masses estimated from X-rays and from weak lensing do not typically show such large offsets. Some systematic discrepancies in the relevant scaling relations were, however, identified and

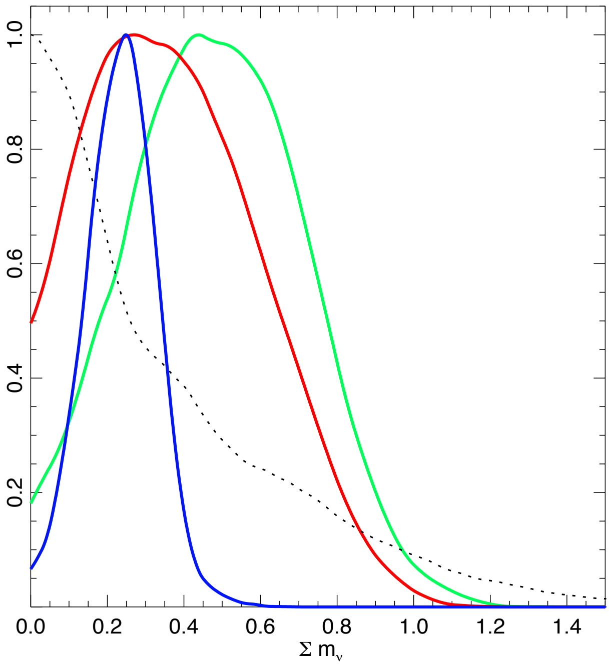

Fig. 12. Cosmological constraints when including neutrino masses $\sum m_\nu$ from: *Planck* CMB data alone (black dotted line); *Planck* CMB + SZ with $1-b$ in [0.7, 1] (red); *Planck* CMB + SZ + BAO with $1-b$ in [0.7, 1] (blue); and *Planck* CMB + SZ with $1-b = 0.8$ (green).

studied in Planck Collaboration XII (2011), Sehgal et al. (2011), Draper et al. (2012), and Biesiadzinski et al. (2012), based on stacking analyses of X-ray, SZ, and lensing data for the very large MaxBCG cluster sample, suggesting that the issue is not yet fully settled from an observational point of view.

A different mass function may also help reconcile the tension. Mass functions are calibrated against numerical simulations that may still suffer from volume effects for the largest halos, as shown in the difference between the Tinker et al. (2008) and Watson et al. (2012) mass functions. This does not seem sufficient, however, given the results presented in Fig. 9.

Alternatively, the discrepancy may indicate the need to extend the minimal ΛCDM model that is used to generate the σ_8 values. Any extension would need to modify the power spectrum on the scales probed by clusters, while leaving the scales probed by primary CMB observations unaffected. The inclusion of neutrino masses, quantified by their sum, $\sum m_\nu$, can achieve this (see Marulli et al. 2011 for a review of how cosmological observations can be affected by the inclusion of neutrino masses). The SPT collaboration (Hou et al. 2012) recently considered such a possibility to mitigate their tension with *WMAP*-7 primary CMB data. There is an upper limit of $\sum m_\nu < 0.93$ eV from the *Planck* primary CMB data alone (Planck Collaboration XVI 2013). If we include the cluster count data using a fixed value $(1-b) = 0.8$, then we find a $2.9\,\sigma$ preference for the inclusion of neutrino masses with $\sum m_\nu = (0.58 \pm 0.20)$ eV, as shown in Fig. 12. If, on the other hand, we adopt a more conservative point of view and allow $(1-b)$ to vary between 0.7 and 1.0, this preference drops to 2σ with $\sum m_\nu = (0.45 \pm 0.21)$ eV. Adding BAO data to the compilation lowers the value of the required mass but increases the significance, yielding $\sum m_\nu = (0.22 \pm 0.09)$ eV, due to a breaking of the degeneracy between H_0 and $\sum m_\nu$.

As these results depends on the value and allowed range of $(1-b)$, better understanding of the scaling relation is the key to further investigation. This provides strong motivation for further study of the relationship between Y and M.

7. Summary

We have used a sample of nearly 200 clusters from the PSZ, along with the corresponding selection function, to place strong constraints in the (Ω_m, σ_8) plane. We have carried out a series of tests to verify the robustness of our constraints, varying the observed sample choice, the estimation method for the selection function, and the theoretical methodology, and have found that our results are not altered significantly by those changes.

The relation between the mass and the integrated SZ signal plays a major role in the computation of the expected number counts. Uncertainties in cosmological constraints from clusters are no longer dominated by small number statistics, but by the gas physics. Uncertainties in the Y–M relation include X-ray instrument calibration, X-ray temperature measurement, inhomogeneities in cluster density or temperature profiles, and selection effects. Considering several ingredients of the gas physics of clusters, numerical simulations predict scaling relations with 30% scatter in amplitude (at a fiducial mass of $6\times10^{14} M_{sol}$). All this points toward a mass bias between the true mass and the estimated mass of $(1-b) = 0.8^{+0.2}_{-0.1}$, and adopting the central value we found constraints on Ω_m and σ_8 that are in good agreement with previous measurements using clusters of galaxies.

Comparing our results with *Planck* primary CMB constraints within the ΛCDM cosmology indicates some tension. This can be alleviated by permitting a large mass bias ($1 - b \simeq 0.55$), which is however significantly larger than expected. Alternatively, the tension may motivate an extension of the ΛCDM model that modifies its power spectrum shape. For example the inclusion of non-zero neutrino masses helps in reconciling the primary CMB and cluster constraints, a fit to *Planck* CMB + SZ + BAO yielding $\sum m_\nu = (0.22 \pm 0.09)$ eV.

Cosmological parameter determination using clusters is currently limited by the knowledge of the observable–mass relations. In the future our goal is to increase the number of dedicated follow-up programmes to obtain better estimates of the mass proxy and redshift for most of the S/N > 5 *Planck* clusters. This will allow for better determination of the scaling laws and the mass bias, increase the number of clusters that can be used, and allow us to investigate an extended cosmological parameter space.

Acknowledgements. The development of *Planck* has been supported by: ESA; CNES and CNRS/INSU-IN2P3-INP (France); ASI, CNR, and INAF (Italy); NASA and DoE (USA); STFC and UKSA (UK); CSIC, MICINN, JA and RES (Spain); Tekes, AoF and CSC (Finland); DLR and MPG (Germany); CSA (Canada); DTU Space (Denmark); SER/SSO (Switzerland); RCN (Norway); SFI (Ireland); FCT/MCTES (Portugal); and PRACE (EU). A description of the *Planck* Collaboration and a list of its members, including the technical or scientific activities in which they have been involved, can be found at http://www.sciops.esa.int/index.php?project=planck&page=Planck_Collaboration

References

Abell, G. O. 1958, ApJS, 3, 211
Abell, G. O., Corwin, Jr., H. G., & Olowin, R. P. 1989, ApJS, 70, 1
Aghanim, N., de Luca, A., Bouchet, F. R., Gispert, R., & Puget, J. L. 1997, A&A, 325, 9
Akritas, M. G. & Bershady, M. A. 1996, ApJ, 470, 706
Allen, S. W., Evrard, A. E., & Mantz, A. B. 2011, Ann.Rev.Astron.Astrophys., 49, 409
Allen, S. W., Evrard, A. E., & Mantz, A. B. 2011, ARA&A, 49, 409
Anderson, L., Aubourg, E., Bailey, S., et al. 2012, MNRAS, 427, 3435

Angulo, R. E., Springel, V., White, S. D. M., et al. 2012, MNRAS, 426, 2046
Arnaud, M., Pointecouteau, E., & Pratt, G. W. 2007, A&A, 474, L37
Arnaud, M., Pratt, G. W., Piffaretti, R., et al. 2010a, A&A, 517, A92
Arnaud, M., Pratt, G. W., Piffaretti, R., et al. 2010b, A&A, 517, A92
Barbosa, D., Bartlett, J. G., Blanchard, A., & Oukbir, J. 1996, A&A, 314, 13
Battaglia, N., Bond, J. R., Pfrommer, C., & Sievers, J. L. 2012, ApJ, 758, 74
Battye, R. A. & Weller, J. 2003, Phys. Rev. D, 68, 083506
Becker, M. R. & Kravtsov, A. V. 2011, ApJ, 740, 25
Benson, B. A., de Haan, T., Dudley, J. P., et al. 2011, ArXiv e-prints
Beutler, F., Blake, C., Colless, M., et al. 2011, MNRAS, 416, 3017
Biesiadzinski, T., McMahon, J., Miller, C. J., Nord, B., & Shaw, L. 2012, ApJ, 757, 1
Birkinshaw, M. 1999, Phys. Rep., 310, 97
Blake, C., Brough, S., Colless, M., et al. 2012, MNRAS, 425, 405
Böhringer, H., Schuecker, P., Guzzo, L., et al. 2004, A&A, 425, 367
Böhringer, H., Voges, W., Huchra, J. P., et al. 2000, ApJS, 129, 435
Carlberg, R. G., Yee, H. K. C., Ellingson, E., et al. 1996, ApJ, 462, 32
Carlstrom, J. E., Ade, P. A. R., Aird, K. A., et al. 2011, PASP, 123, 568
Cash, W. 1979, ApJ, 228, 939
da Silva, A. C., Kay, S. T., Liddle, A. R., & Thomas, P. A. 2004, MNRAS, 348, 1401
Diego, J. M., Martínez-González, E., Sanz, J. L., Benitez, N., & Silk, J. 2002, MNRAS, 331, 556
Draper, P., Dodelson, S., Hao, J., & Rozo, E. 2012, Phys. Rev. D, 85, 023005
Fabjan, D., Borgani, S., Rasia, E., et al. 2011, MNRAS, 416, 801
Haiman, Z., Mohr, J. J., & Holder, G. P. 2001, ApJ, 553, 545
Hasselfield, M., Hilton, M., Marriage, T. A., et al. 2013, ArXiv e-prints
Hinshaw, G., Larson, D., Komatsu, E., et al. 2012, ArXiv e-prints
Holder, G., Haiman, Z., & Mohr, J. J. 2001, ApJ, 560, L111
Hou, Z., Reichardt, C. L., Story, K. T., et al. 2012, ArXiv e-prints
Kay, S. T., Peel, M. W., Short, C. J., et al. 2012a, MNRAS, 422, 1999
Kay, S. T., Peel, M. W., Short, C. J., et al. 2012b, MNRAS, 422, 1999
Kilbinger, M., Fu, L., Heymans, C., et al. 2013, MNRAS, 735
Krause, E., Pierpaoli, E., Dolag, K., & Borgani, S. 2012, MNRAS, 419, 1766
Kravtsov, A. V., Vikhlinin, A., & Nagai, D. 2006, ApJ, 650, 128
Lau, E. T., Kravtsov, A. V., & Nagai, D. 2009, ApJ, 705, 1129
Lewis, A. & Bridle, S. 2002, Phys. Rev., D66, 103511
Lewis, A., Challinor, A., & Lasenby, A. 2000, Astrophys. J., 538, 473
Mahdavi, A., Hoekstra, H., Babul, A., et al. 2012, ArXiv e-prints
Mahdavi, A., Hoekstra, H., Babul, A., & Henry, J. P. 2008, MNRAS, 384, 1567
Marrone, D. P., Smith, G. P., Okabe, N., et al. 2012, ApJ, 754, 119
Marulli, F., Carbone, C., Viel, M., Moscardini, L., & Cimatti, A. 2011, MNRAS, 418, 346
Mazzotta, P., Rasia, E., Moscardini, L., & Tormen, G. 2004, MNRAS, 354, 10
Mehrtens, N., Romer, A. K., Hilton, M., et al. 2012, MNRAS, 423, 1024
Melin, J., Bartlett, J. G., & Delabrouille, J. 2006, A&A, 459, 341
Meneghetti, M., Rasia, E., Merten, J., et al. 2010, A&A, 514, A93
Motl, P. M., Hallman, E. J., Burns, J. O., & Norman, M. L. 2005, ApJ, 623, L63
Nagai, D. 2006a, ApJ, 650, 538
Nagai, D. 2006b, ApJ, 650, 538
Nagai, D., Kravtsov, A. V., & Vikhlinin, A. 2007, ApJ, 668, 1
Padmanabhan, N., Xu, X., Eisenstein, D. J., et al. 2012, MNRAS, 427, 2132
Piffaretti, R. & Valdarnini, R. 2008, A&A, 491, 71
Planck Collaboration I. 2013, In preparation
Planck Collaboration Int. I. 2012, A&A, 543, A102
Planck Collaboration Int. III. 2013, A&A, 550, A129
Planck Collaboration Int. IV. 2013, A&A, 550, A130
Planck Collaboration IX. 2011, A&A, 536, A9
Planck Collaboration VIII. 2011, A&A, 536, A8
Planck Collaboration X. 2011, A&A, 536, A10
Planck Collaboration XI. 2011, A&A, 536, A11
Planck Collaboration XII. 2011, A&A, 536, A12
Planck Collaboration XV. 2013, In preparation
Planck Collaboration XVI. 2013, In preparation
Planck Collaboration XXI. 2013, In preparation
Planck Collaboration XXIX. 2013, In preparation
Pratt, G. W., Croston, J. H., Arnaud, M., & Böhringer, H. 2009, A&A, 498, 361
Rasia, E., Meneghetti, M., Martino, R., et al. 2012, New Journal of Physics, 14, 055018
Reichardt, C. L., Stalder, B., Bleem, L. E., et al. 2012a, ArXiv e-prints
Reichardt, C. L., Stalder, B., Bleem, L. E., et al. 2012b, ArXiv e-prints
Riess, A. G., Macri, L., Casertano, S., et al. 2011, ApJ, 730, 119
Rozo, E., Vikhlinin, A., & More, S. 2012, ApJ, 760, 67
Rozo, E., Wechsler, R. H., Rykoff, E. S., et al. 2010, ApJ, 708, 645
Sehgal, N., Bode, P., Das, S., et al. 2010, ApJ, 709, 920
Sehgal, N., Trac, H., Acquaviva, V., et al. 2011, ApJ, 732, 44
Springel, V., White, M., & Hernquist, L. 2001, ApJ, 562, 1086
Steigman, G. 2008, ArXiv e-prints
Story, K. T., Reichardt, C. L., Hou, Z., et al. 2012, ArXiv e-prints
Sunyaev, R. A. & Zeldovich, Y. B. 1970, Ap&SS, 7, 20
Swetz, D. S., Ade, P. A. R., Amiri, M., et al. 2011, ApJS, 194, 41
Taburet, N., Aghanim, N., Douspis, M., & Langer, M. 2009, MNRAS, 392, 1153
Taburet, N., Douspis, M., & Aghanim, N. 2010, MNRAS, 404, 1197
Tinker, J., Kravtsov, A. V., Klypin, A., et al. 2008, ApJ, 688, 709
Vikhlinin, A., Burenin, R. A., Ebeling, H., et al. 2009a, ApJ, 692, 1033
Vikhlinin, A., Kravtsov, A. V., Burenin, R. A., et al. 2009b, ApJ, 692, 1060
Vikhlinin, A., Kravtsov, A. V., Burenin, R. A., et al. 2009c, ApJ, 692, 1060
Voit, G. M. 2005, Reviews of Modern Physics, 77, 207
von der Linden, A., Allen, M. T., Applegate, D. E., et al. 2012, ArXiv e-prints
Watson, W. A., Iliev, I. T., D'Aloisio, A., et al. 2012, ArXiv e-prints
Weller, J., Battye, R. A., & Kneissl, R. 2002, Physical Review Letters, 88, 231301
White, S. D. M., Navarro, J. F., Evrard, A. E., & Frenk, C. S. 1993, Nature, 366, 429
Willis, J. P., Clerc, N., Bremer, M. N., et al. 2013, MNRAS, 620
Yang, H.-Y. K., Bhattacharya, S., & Ricker, P. M. 2010, ApJ, 725, 1124
Zeldovich, Y. B. & Sunyaev, R. A. 1969, Ap&SS, 4, 301
Zhang, Y.-Y., Okabe, N., Finoguenov, A., et al. 2010, ApJ, 711, 1033

Appendix A: Calibration of the Y_{500}–M_{500} relation

A cluster catalogue is a list of positions and measurements of observable physical quantities. Its scientific utility depends largely on our ability to link the observed quantities to the underlying mass, in other words, to define an observable proxy for the mass. *Planck* detects clusters through the SZ effect. This effect is currently the subject of much study in the cluster community, chiefly because numerical simulations indicate that the spherically-integrated SZ measurement is correlated particularly tightly with the underlying mass. In other words, this measurement potentially represents a particularly valuable mass proxy.

To establish a mass proxy, one obviously needs an accurate measurement both of the total mass and of the observable quantity in question. However, even with highly accurate measurements, the correlation between the observable quantity and the mass is susceptible to *bias* and *dispersion*, and both of these effects need to be taken into account when using cluster catalogues for scientific applications.

The aim of this Appendix is to define a baseline relation between the measured SZ flux, Y_{500}, and the total mass M_{500}. The latter quantity is not directly measurable. On an individual cluster basis, it can be inferred from dynamical analysis of galaxies, from X-ray analysis assuming hydrostatic equilibrium (HE), or from gravitational lensing observations. However, it is important to note that *all* observed mass estimates include inherent biases. For instance, numerical simulations suggest that HE mass measurements are likely to underestimate the true mass by 10–15 percent due to neglect of bulk motions and turbulence in the intra-cluster medium ((ICM, e.g., Nagai et al. 2007; Piffaretti & Valdarnini 2008; Meneghetti et al. 2010)), an effect that is commonly referred to in the literature as the "hydrostatic mass bias". Similarly, simulations indicate that weak lensing mass measurements may be biased by 5 to 10 percent, owing to projection effects or the use of inappropriate mass models (e.g., Becker & Kravtsov 2011). Instrument calibration systematic effects constitute a further source of error. For X-ray mass determinations, temperature estimates represent the main source of systematic uncertainty, as the mass at a given density contrast scales roughly with $T^{3/2}$. Other biases in the determination of mass–observable scaling relations come from the object selection process itself (e.g., Allen et al. 2011; Angulo et al. 2012). A classic example is the Malmquist bias, where bright objects near the flux limit are preferentially detected. This effect is amplified by Eddington bias, the mass function dictating that many more low-mass objects are detected compared to high-mass objects. Both of these biases depend critically on the distribution of objects in mass and redshift, and on the dispersion in the relation between the mass and the observable used for sample selection. This is less of a concern for SZ selected samples than for X-ray selected samples, the SZ signal having much less scatter at a given mass than the X-ray luminosity. However for precise studies it should still be taken into account.

On the theoretical side, numerous Y_{500}–M_{500} relations have been derived from simulated data, as discussed below. The obvious advantage of using simulated data is that the relation between the SZ signal and the true mass can be obtained, because the 'real' value of all physical quantities can be measured. The disadvantage is that the 'real' values of measurable physical quantities depend strongly on the phenomenological models used to describe the different non-gravitational processes at work in the ICM.

Nevertheless, the magnitude of the bias between observed and true quantities can only be assessed by comparing multi-wavelength observations, of a well-controlled cluster sample, to numerical simulations. Thus, ideally, we would have full follow-up of a complete *Planck* cluster sample. For large samples, however, full follow-up is costly and time consuming. This has led to the widespread use of mass estimates obtained from mass–proxy relations. These relations are generally calibrated from individual deep observations of a subset of the sample in question (e.g., Vikhlinin et al. 2009a), or from deep observations of objects from an external dataset (e.g., use of the REXCESS relations in Planck Collaboration XI 2011).

For the present paper, we will rely on mass estimates from a mass–proxy relation. In this context, the M_{500}–Y_X relation is clearly the best to use. Y_X, proposed by Kravtsov et al. (2006), is defined as the product of $M_{g,500}$, the gas mass within R_{500}, and T_X, the spectroscopic temperature measured in the [0.15–0.75] R_{500} aperture. In the simulations performed by Kravtsov et al. (2006), Y_X was extremely tightly correlated with the true cluster mass, with a logarithmic dispersion of only 8 percent. Observations using masses derived from X-ray hydrostatic analysis indicate that Y_X does indeed appear to have a low dispersion (Arnaud et al. 2007; Vikhlinin et al. 2009a). Furthermore, the local M_{500}–Y_X relation for X-ray selected relaxed clusters has been calibrated to high statistical precision (Arnaud et al. 2010b; Vikhlinin et al. 2009a), with excellent agreement achieved between various observations (see e.g., Arnaud et al. 2007). Since simulations suggest that the Y_{500}–M_{500} relation is independent of dynamical state, calibrating the Y_{500}–M_{500} relation via a low-scatter mass proxy, itself calibrated on clusters for which the HE bias is expected to be minimal, is a better approach than using HE mass estimates for the full sample, since the latter can be highly biased for very unrelaxed objects.

We approach the determination of the Y_{500}–M_{500} relation in two steps. We first calibrate the Y_{500}–proxy relation. This is combined with the X-ray calibrated relation, between the proxy and M_{500}, to define an observation-based Y_{500}–M_{500} relation. In the second step, we assess possible biases on the relation by directly comparing the observation-based relation with that from simulations. This approach, rather than directly assessing the HE mass bias, allows us to avoid complications linked to the strong dependence of the HE bias on cluster dynamical state, and thus on the cluster sample (real or simulated). The final output from this procedure is a relation between Y_{500} and M_{500}, with a full accounting of the different statistical and systematic uncertainties that go into its derivation, including bias.

In the following, all relations are fit with a power law in log-space using orthogonal the BCES method (Akritas & Bershady 1996), which takes into account the uncertainties in both variables and the intrinsic scatter. All dispersions are given in $\log_{10}$.

A.1. Baseline mass–proxy relation

As a baseline, we use the relation between Y_X and the X-ray hydrostatic mass M_{500}^{HE} established for 20 local *relaxed* clusters by Arnaud et al. (2010b):

$$E^{-2/3}(z)\left[\frac{Y_X}{2\times10^{14}\mathrm{M_{sol}\,keV}}\right] = 10^{0.376\pm0.018}\left[\frac{M_{500}^{HE}}{6\times10^{14}\mathrm{M_{sol}}}\right]^{1.78\pm0.06}, \quad (A.1)$$

assuming standard evolution, and where the uncertainties are statistical only. For easier comparison with the Y_{500}–M_{500} relation given below, the normalization for Y_X expressed in 10^{-4} Mpc^2 is $10^{-0.171\pm0.018}$. The HE mass is expected to be a biased estimator of the true mass,

$$M_{500}^{HE} = (1-b)\,M_{500}\,, \quad (A.2)$$

where all of the possible observational biases discussed above (departure from HE, absolute instrument calibration, temperature inhomogeneities, residual selection bias) have been subsumed into the bias factor $(1-b)$. The form of the Y_X–M_{500} relation is thus

$$E^{-2/3}(z)Y_X = 10^{A\pm\sigma_A}\,[(1-b)\,M_{500}]^{\alpha\pm\sigma_\alpha}\,, \quad (A.3)$$

where σ_A and σ_α are the statistical uncertainties on the normalization and slope and b is the bias between the true mass and the observed mass used to calibrate the relation. The bias is a poorly-known stochastic variable with substantial variation expected between clusters. In our case, b represents the *mean* bias between the observed mass and the true mass.

The mass proxy $M_{500}^{Y_X}$ is defined from the best-fit Y_X–M_{500}^{HE} relation

$$E^{-2/3}(z)Y_X = 10^{A}\left[M_{500}^{Y_X}\right]^{\alpha}. \quad (A.4)$$

For any cluster, $M_{500}^{Y_X}$, together with the corresponding Y_X and $R_{500}^{Y_X}$, can be estimated iteratively about this relation from the observed temperature and gas mass profile, as described in Kravtsov et al. (2006). The calibration of the Y_X–M_{500} relation is equivalent to a calibration of the $M_{500}^{Y_X}$–M_{500} relation, which relates the mass proxy, $M_{500}^{Y_X}$, to the mass via

$$M_{500}^{Y_X} = 10^{\pm\sigma_A/\alpha}\,[(1-b)\,M_{500}]^{1\pm\sigma_\alpha/\alpha}\,. \quad (A.5)$$

In addition to the bias factor, there are statistical uncertainties on the slope and normalization of the relation, as well as intrinsic scatter around the relation, linked to the corresponding statistical uncertainties and scatter of the Y_X–M_{500}^{HE} relation.

A.2. Relation between Y_{500} and $M_{500}^{Y_X}$

A.2.1. Best-fit relation

We first investigate the relationship between Y_{500} and $M_{500}^{Y_X}$, the mass estimated iteratively from Eq. A.4, with parameters given by the best-fit Arnaud et al. (2010b) relation (Eq. A.2). Full X-ray follow-up of the *Planck* SZ cosmological cluster

Table A.1. Parameters for the Y_{500}–M_{500} relation, expressed as $E^{-2/3}(z)\left[D_A^2 Y_{500}/10^{-4}\mathrm{Mpc}^2\right] = 10^{\alpha}\left[M_{500}/6\times10^{14}\mathrm{M_{sol}}\right]^{\beta}$: column 1, considered sample; column 2, number of clusters in the sample; column 3, Malmquist bias correction; if this column contains Y, a mean correction for Malmquist bias has been applied to each point before fitting; column 4, Mass definition; columns 5 and 6, slope and normalization of the relation; columns 7 and 8, intrinsic and raw scatter around the best-fit relation.

Sample	N_c	MB	Mass	α	β	$\sigma_{\log,\mathrm{int}}$	$\sigma_{\log,\mathrm{raw}}$
XMM-ESZ PEPXI	62	N	$M_{500}^{Y_X}$	-0.19 ± 0.01	1.74 ± 0.08	0.10 ± 0.01	...
Cosmo sample	71	N	$M_{500}^{Y_X}$	-0.175 ± 0.011	1.77 ± 0.06	0.065 ± 0.010	0.080 ± 0.009
Cosmo sample	**71**	**Y**	$M_{500}^{Y_X}$	$\mathbf{-0.186 \pm 0.011}$	$\mathbf{1.79 \pm 0.06}$	$\mathbf{0.063 \pm 0.011}$	$\mathbf{0.079 \pm 0.009}$
XMM-ESZ	62	Y	$M_{500}^{Y_X}$	-0.19 ± 0.01	1.75 ± 0.07	0.065 ± 0.011	0.079 ± 0.009
S/N > 7	78	Y	$M_{500}^{Y_X}$	-0.18 ± 0.01	1.72 ± 0.06	0.063 ± 0.010	0.078 ± 0.008
Cosmo sub-sample A	10	Y	M_{500}^{HE}	-0.15 ± 0.04	1.6 ± 0.3	...	0.08 ± 0.02
Cosmo sub-sample B	56	Y	M_{500}^{HE}	-0.19 ± 0.03	1.7 ± 0.2	0.25 ± 0.06	0.27 ± 0.06

sample is not yet available. Our baseline sample is thus a subset of 71 detections from the *Planck* cosmological cluster sample, detected at S/N > 7, for which good quality *XMM-Newton* observations are available. The sample consists of data from our previous archival study of the *Planck* Early SZ (ESZ) clusters (Planck Collaboration XI 2011), of *Planck*-detected LoCuSS clusters presented by Planck Collaboration Int. III (2013), and from the *XMM-Newton* validation programme (Planck Collaboration IX 2011; Planck Collaboration Int. I 2012; Planck Collaboration Int. IV 2013). The corresponding sub-samples include 58, 4, and 9 clusters, respectively. Uncertainties on Y_X, $R_{500}^{Y_X}$, and $M_{500}^{Y_X}$ include those due to statistical errors on the X-ray temperature and the gas mass profile.

The SZ signal is estimated within a sphere of radius $R_{500}^{Y_X}$ centred on the position of the X-ray peak, as detailed in e.g., Planck Collaboration XI (2011). The re-extraction procedure uses Matched Multi-Filters (MMF) and assumes that the ICM pressure follows the universal profile shape derived by Arnaud et al. (2010b) from the combination of the REXCESS sample with simulations. The uncertainty on Y_{500} includes statistical uncertainties on the SZ signal derived from the MMF, plus the statistical uncertainty on the aperture $R_{500}^{Y_X}$. The latter uncertainty is negligible compared to the statistical error on the SZ signal. The resulting relation for these 71 clusters from the cosmological sample is

$$E^{-2/3}(z)\left[\frac{D_A^2\, Y_{500}}{10^{-4}\,\mathrm{Mpc}^2}\right] = 10^{-0.175\pm0.011}\left[\frac{M_{500}^{Y_X}}{6\times10^{14}\mathrm{M_{sol}}}\right]^{1.77\pm0.06}. \quad \text{(A.6)}$$

This agrees within 1σ with the results from the sample of 62 clusters from the ESZ sample with archival *XMM-Newton* data published in Planck Collaboration XI (2011). The slope and normalization are determined at slightly higher precision, due to the better quality SZ data. The derived intrinsic scatter (Table A.1) is significantly smaller. This is a consequence of: a more robust treatment of statistical uncertainties; propagation of gas mass profile uncertainties in the Y_X error budget; and, to a lesser extent, the propagation of $R_{500}^{Y_X}$ uncertainties to Y_{500} estimates.

A.2.2. Effects of Malmquist bias

The fitted parameters are potentially subject to selection effects such as Malmquist bias, owing to part of the sample lying close to the selection cut. For the present sample, we use an approach adapted from that described in Vikhlinin et al. (2009a) and Pratt et al. (2009), where each data point is rescaled by the mean bias for its flux, and the relation refitted using the rescaled points. The method is described in more detail in Paper 1. For the baseline cosmological sample of 71 systems, the bias-corrected Y_{500}–$M_{500}^{Y_X}$ relation is

$$E^{-2/3}(z)\left[\frac{D_A^2\, Y_{500}}{10^{-4}\,\mathrm{Mpc}^2}\right] = 10^{-0.19\pm0.01}\left[\frac{M_{500}^{Y_X}}{6\times10^{14}\mathrm{M_{sol}}}\right]^{1.79\pm0.06}. \quad \text{(A.7)}$$

The best-fit relation, together with Malmquist bias corrected data points, is plotted in Fig. A.1.

The correction decreases the effective Y_{500} values at a given mass, an effect larger for clusters closer to the S/N threshold. The net effect is small, a roughly $1\,\sigma$ decrease of the normalization and a slight steepening of the power-law slope (Table A.1).

A.2.3. Stability of slope and normalization

We note that the slope and normalization of this relation are robust to the choice of sample (Table A.1). There is agreement within $1\,\sigma$ with the results derived from the extended sample of 78 clusters having S/N > 7 with archive *XMM-Newton* observations and the updated XMM-ESZ sample. They are also in agreement with the relation obtained from a simple combination of the Y_{500}–Y_X relation (discussed in Paper 1) and the Y_X–M_{500}^{HE} relation (Eq. A.2 above).

A.3. The observation-based Y_{500}–M_{500} relation

A.3.1. Combination of the Y_{500}–$M_{500}^{Y_X}$ and the $M_{500}^{Y_X}$–M_{500} relations

We now combine Eq. A.8 with the $M_{500}^{Y_X}$–M_{500} relation. This will not change the best-fit parameters, but will increase their uncertainties. As the determinations of the two relations are independent, we added quadratically the uncertainties in the best-fit parameters of the Y_{500}–$M_{500}^{Y_X}$ (Eq. A.7) and $M_{500}^{Y_X}$–M_{500} (Eq. A.5,

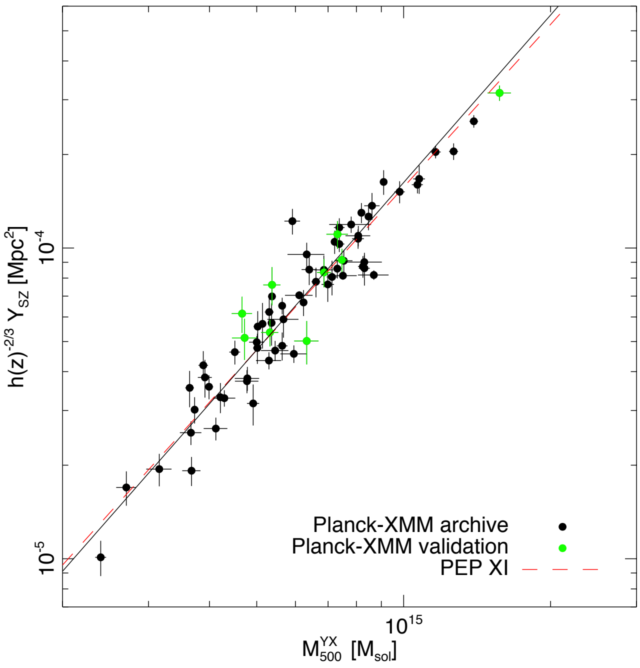

Fig. A.1. Best scaling relation between Y_{500} and M_{500}, and the data points utilized after correction of the Malmquist bias

with values from Eq. A.2) relations. Our best-fit Y_{500}–M_{500} relation is then

$$E^{-2/3}(z)\left[\frac{D_A^2\,Y_{500}}{10^{-4}\,\mathrm{Mpc}^2}\right] = 10^{-0.19\pm0.02}\left(\frac{(1-b)\,M_{500}}{6\times10^{14}\mathrm{M_{sol}}}\right)^{1.79\pm0.08}. \quad \text{(A.8)}$$

Thus inclusion of the statistical uncertainty in the $M_{500}^{Y_X}$–M_{500}^{HE} relation doubles the uncertainty on the normalization and increases the uncertainty on the slope by 40%.

A.3.2. Effect of use of an external dataset

The above results assume a mass estimated from the baseline Y_X–M_{500} relation, derived by Arnaud et al. (2010b) from an external dataset of 20 relaxed clusters (Eq A.2). How does this relation compare to the individual hydrostatic X-ray masses of the *Planck* cosmological cluster sample? While spatially-resolved temperature profiles are available for 58 of the 71 clusters with *XMM-Newton* observations, we must be careful in interpretation of these data. The Arnaud et al. relation was derived from a carefully chosen data set consisting of relaxed, cool-core objects having well-constrained temperature profiles out to around R_{500}, i.e., the type of object for which it makes sense to undertake a hydrostatic mass analysis. Many clusters of the *Planck* sample are merging systems for which such an analysis would give results that are difficult to interpret. In addition, few of the *Planck* sample have spatially-resolved temperature profiles out to R_{500}. However, as given in Table A.1, the best-fit Y_X–M_{500}^{HE} relation for the 10 cool-core clusters that are detected to R_{500} agrees with Eq. A.9 within 1 σ. Moreover, the relation for the 58 *Planck* clusters with HE mass estimates, regardless of dynamical state, also agrees within 1 σ (albeit with greatly increased scatter). We are thus confident that the masses estimated from an externally-calibrated Y_X–M_{500}^{HE} relation are applicable to the present data set.

A.3.3. Dispersion about the observed relations

A key issue is the dispersion around the mean relation. We first estimate an upper limit[6] to the intrinsic scatter of the Y_{500}–M_{500}^{HE} relation by combining the intrinsic scatter of the Y_{500}–$M_{500}^{Y_X}$ relation and that of the $M_{500}^{Y_X}$–M_{500}^{HE} relation. This upper limit is applicable to relaxed objects only, since the Y_{500}–M_{500}^{HE} relation has been measured using a sample of such systems. This gives

$$\sigma = \sqrt{\sigma^2_{\mathrm{Y_{500}|M_{500}^{Y_X}}} + 2\cos^2(\tan^{-1}\beta)\,\sigma^2_{\mathrm{M_{500}^{HE}|Y_X}}}\,, \quad \text{(A.9)}$$

where β is the slope of the Y_{500}–$M_{500}^{Y_X}$ relation. As the HE mass estimate introduces extra scatter as compared to the true mass (Kay et al. 2012b), the dispersion about the Y_{500}–M_{500} relation is expected to be smaller than that of the Y_{500}–M_{500}^{HE} relation. The above expression thus also provides an upper limit to the scatter of the Y_{500}–M_{500} relation, again for relaxed objects. Further assuming that the intrinsic scatter of the Y_{500}–M_{500} relation is the same for the total relaxed and unrelaxed population, as indicated by numerical simulations (Kravtsov et al. 2006; Kay et al. 2012b), Eq. A.9 gives a conservative estimate of the intrinsic scatter of the Y_{500}–M_{500} relation.

The intrinsic dispersion about our baseline Y_X–M_{500}^{HE} relation (Eq. A.2), taken from Arnaud et al. (2010b), is not measurable; neither is it measurable for the best-fit *Chandra* Y_X–M_{500}^{HE} relation published in Vikhlinin et al. (2009a). Using a smaller sample of 10 systems, Arnaud et al. (2007) measured an intrinsic scatter of $\sigma_{\log \mathrm{M_{500}^{HE}|Y_X}} = 0.039$ (9 percent), in excellent agreement with the results of the simulations of Nagai et al. (2007) for the scatter of the M_{500}^{HE}–Y_X relation for relaxed clusters (8.7 percent, their Table 4). It is somewhat larger than the intrinsic scatter of the relation between the true mass and Y_X derived by Kravtsov et al. ($\sigma_{\log \mathrm{M_{500}|Y_X}} = 5-7$ percent) but close to the results of Fabjan et al. (2011), who find $\sigma_{\log \mathrm{M_{500}|Y_X}}$ =0.036-0.046. We thus take as a conservative estimate $\sigma_{\log \mathrm{M_{500}^{HE}|Y_X}} = 0.05$. The intrinsic dispersion about the Y_{500}–$M_{500}^{Y_X}$ relation for our data is $\sigma_{\log \mathrm{Y_{500}|M_{500}^{Y_X}}} = 0.065 \pm 0.01$. This value is three times larger than the results of Kay et al. (2012b). Partly this is due to the presence of outliers in our dataset (as discussed in Paper 1), and it may also be due to projection effects in observed data sets (Kay et al. 2012b).

Our final upper limit on the intrinsic scatter is then $\sigma_{\log \mathrm{Y_{500}|M_{500}}} < 0.074$ or 18 percent, similar to the predictions from Kay et al. (2012b) and Sehgal et al. (2010). These predictions depend both on the numerical scheme and specific physics assumptions, with values varying by a factor of two in the typical range 0.04 to 0.08 (references in Sect. A.4.1 below).

A.4. Assessing the bias from comparison with numerical simulations

The final piece of the jigsaw consists of assessing the bias b in Eq. A.2. Since the relation has been calibrated using the HE mass for a sample of *relaxed clusters*, b represents the bias between M_{500}^{HE} and the true mass for this category of clusters. In principle, this can be assessed through comparison with numerical simulations. However, this approach is hampered by two difficulties.

[6] When combining relations of the type $Z = BY^{\beta}$ and $Y = AX^{\alpha}$, the *orthogonal* scatter of the Z–X relation is the quadratic sum of the orthogonal scatter of the individual relations, if Y is a fully independent variable. In other cases, this provides an upper limit.

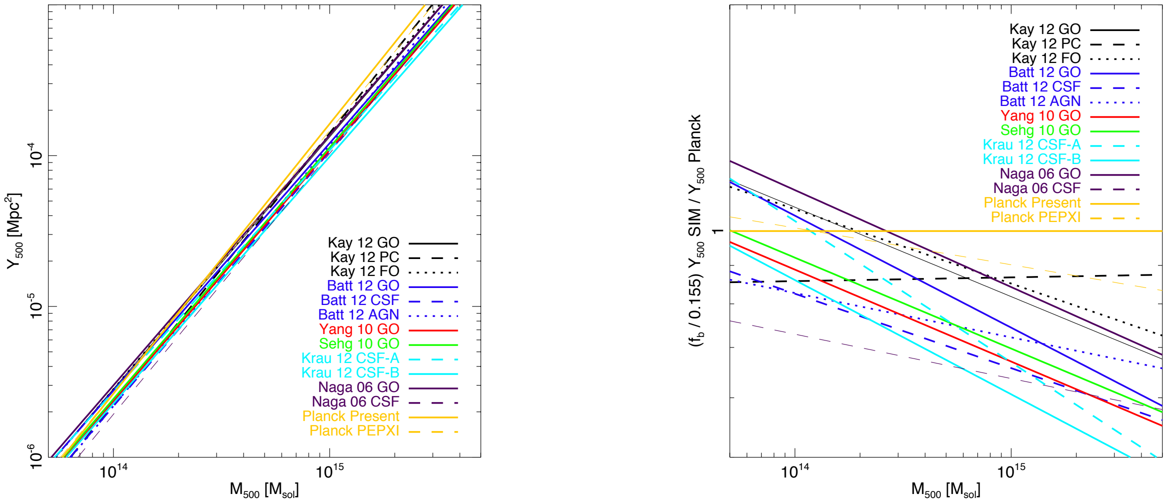

Fig. A.2. *Left:* comparison of Y_{500}–M_{500} relations from 12 simulations undertaken by six different groups with the updated observational Y_{500}–$M_{500}^{\rm HE}$ result from *Planck*, Eq. A.9. *Right:* ratio of each simulated Y_{500}–M_{500} relation relative to Eq. A.9. The different scaling laws are taken from Kay et al. (2012b), Battaglia et al. (2012), Yang et al. (2010), Sehgal et al. (2010), Krause et al. (2012), Nagai (2006b), and Planck Collaboration XI (2011).

The first is the exact definition of "relaxed", since it is almost impossible to select such clusters from observations and simulations according to the *same* criteria. The second is the specific implementation of the HE equation, which can differ substantially between observations (e.g., the use of forward fitting using parametric models, etc.) and simulations (e.g., the use of mock observations, etc.). Thus the amplitude of the bias that is found will depend not only on physical departures from HE, but also on technical details in the approach to data analysis.

Here we use a different approach that avoids these pitfalls, assessing the bias b by comparing directly the estimated Y_{500}–M_{500} relations with those found from numerical simulations. We then discuss the consistency of the resulting bias estimate with the HE bias expected from simulations and from absolute calibration uncertainties.

A.4.1. Comparison of simulated Y_{500}–M_{500} relations and data

We first compared the Y_{500}–M_{500} relations from 12 different analyses done by six groups (Nagai 2006b; Yang et al. 2010; Sehgal et al. 2010; Krause et al. 2012; Battaglia et al. 2012; Kay et al. 2012b). We translated the results into a common cosmology and, where necessary, converted cylindrical relations into spherical measurements assuming a ratio of $Y_{500,\rm cyl}/Y_{500,\rm sph} = 0.74/0.61 \simeq 1.2$, as given by the Arnaud et al. (2010b) pressure profile.

The left-hand panel of Fig. A.2 shows the different Y_{500}–M_{500} relations rescaled to our chosen cosmology. The simulations use various different types of input physics, and the resulting Y_{500}–M_{500} relations depend strongly on this factor. The only obvious trend is a mild tendency for adiabatic simulations to find nearly self-similar slopes (1.66). Runs with non-gravitational processes tend to find slightly steeper slopes, but this is not always the case (e.g., the Krause et al. 2012 simulations). The right-hand panel of Fig. A.2 shows the *ratio* of each simulation Y_{500}–M_{500} relation to the *Planck* Y_{500}–$M_{500}^{Y_{\rm X}}$ relation given in Eq. A.9. All results have been rescaled to account for the differences in baryon fraction between simulations. At our reference pivot point of $M_{500} = 6\times10^{14}\,{\rm M_{sol}}$, all simulations are offset from the measured relation. There is also a clear dependence on mass arising from the difference in slope between the majority of the simulated relations and that of the *Planck* relation. The *Planck* slope is steeper, possibly indicating the stronger effect of non-gravitational processes in the real data.

A.4.2. Quantification of the mass bias

We define the mass bias b between the "true" and observed M_{500} values, following Eq. A.2. Both masses are defined at a fixed density contrast of 500, so that the relations between observed and true mass and radius read

$$\begin{aligned} M_{500}^{\rm obs} &= (1-b)\,M_{500}^{\rm true}\,, \\ R_{500}^{\rm obs} &= (1-b)^{1/3}\,R_{500}^{\rm true}\,, \end{aligned} \quad (A.10)$$

where 'true' denotes simulated quantities, and "obs" denotes quantities estimated at the apertures derived from observations. In our case, Y_{500} is measured interior to $R_{500}^{Y_{\rm X}}$ as opposed to $R_{500}^{\rm true}$. The corresponding Y_{500}–M_{500} relations are

$$Y(< R_{500}^{\rm true}) = A_{\rm true}\left[M_{500}^{\rm true}\right]^{5/3}\,, \quad (A.11)$$

$$Y(< R_{500}^{\rm obs}) = A_{\rm obs}\left[M_{500}^{\rm obs}\right]^{5/3}\,, \quad (A.12)$$

neglecting any departure from the self-similar slope.

The bias b can then be estimated from the ratio of the normalization of the observed and simulated relations:

$$\frac{A_{\rm true}}{A_{\rm obs}} = \frac{Y(< R_{500}^{\rm true})}{Y(< R_{500}^{\rm obs})}\left[\frac{M_{500}^{\rm obs}}{M_{500}^{\rm true}}\right]^{5/3} \propto f(b)\times(1-b)^{5/3}\,, \quad (A.13)$$

where $f(b)$ depends on the radial variation of Y_{500} for scaled radii, $r/R_{500}^{Y_{\rm X}} = R_{500}^{\rm true}/R_{500}^{\rm obs} = (1-b)^{-1/3}$, which is close to 1. For a GNFW universal profile (Arnaud et al. 2010b), we find that $f(b)$ can be well fit by a power law of the form $(1-b)^{-1/4}$. Thus we arrive at

$$(1-b) = (A_{\rm true}/A_{\rm obs})^{12/17}\,. \quad (A.14)$$

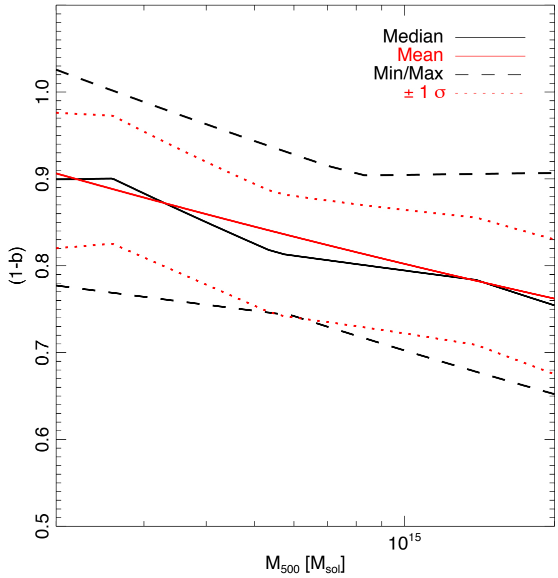

Fig. A.3. The dependence of $(1-b)$ on mass. Note that this value is strongly dependent on the baryon fraction f_b (see text).

For the ensemble of simulations shown in Fig. A.2, we have measured the values of A_{true}/A_{obs} for various values of M_{true}. Figure A.3 shows the variation of $(1-b)$ as a function of mass M. This is mass-dependent due to the difference in slopes between the simulated and observed relations. At a pivot point of $M_{500} = 6\times10^{14}$ M_{sol}, the median value of A_{true}/A_{obs} is 0.74, implying $(1-b) = 0.81$. However, there is a large amount of scatter in the predictions from simulations. As a consequence, $(1-b)$ can vary from 0.74 to 0.97 at $M_{500} = 6\times10^{14}$ M_{sol}. Note that the above results depend significantly on the baryon fraction f_b. For example, assuming the *WMAP*-7 value $f_b = 0.167$, the median value of $(1-b)$ is 0.86 at the pivot point of $M_{500} = 6\times10^{14}$ M_{sol}.

A.4.3. Consistency with HE bias predictions and absolute calibration uncertainties

Taken at face value, the bias we derive above of $(1-b) \simeq 0.8$ implies that the HE mass used to calibrate the Y_{500}–M_{500}^{HE} relation is offset from the true mass by around 20 percent. Is this reasonable?

We can first compare HE X-ray and weak lensing (WL) masses. Although as mentioned above both measurements are expected to be biased, such comparisons are useful because the mass measurements involved are essentially independent. In addition measurements for moderately large sample sizes (tens of systems) are now starting to appear in the literature. However, at present there is little consensus, with some studies finding good agreement between HE and WL masses (e.g., Vikhlinin et al. 2009a; Zhang et al. 2010), some finding that HE masses are lower than WL masses, (e.g., Mahdavi et al. 2008), and some even finding that HE masses are higher than WL masses (Planck Collaboration Int. III 2013). The key point in such analyses is rigorous data quality on both the X-ray and optical sides. The most recent works both point to relatively good agreement between X-ray and WL masses, with $M^{HE}/M^{WL} \simeq 0.9$ on average, and $M^{HE}/M^{WL} \simeq 1$ for relaxed systems (Mahdavi et al. 2012; von der Linden et al. 2012).

According to cosmological numerical simulations, the measurement bias induced by X-ray measurements relative to the "true" values can be caused by two main effects. The first is the classic "hydrostatic bias" due to non-thermal pressure support from turbulence/random motions, etc. However, the exact details are very model-dependent. The HE bias expected from simulations varies substantially, depending on the details of the numerical scheme, the input physics, and the approach used to calculate the HE masses (e.g., Rasia et al. 2012). In addition, the amount of bias is different depending on the dynamical state of the object, relaxed systems having less bias than unrelaxed systems. The majority of numerical simulations predict HE biases of 10 to 20 percent (Nagai et al. 2007; Piffaretti & Valdarnini 2008; Lau et al. 2009; Kay et al. 2012b; Rasia et al. 2012).

Temperature inhomogeneities constitute the second contributor to X-ray measurement bias. In the presence of large amounts of cool gas, a single-temperature fit to a multi-temperature plasma will yield a result that is biased towards lower temperatures (e.g., Mazzotta et al. 2004). The presence of temperature inhomogeneities will depend on the dynamical state. While this effect can be investigated with simulations, estimates of its impact vary widely, owing to differences in numerical schemes and the different implementations of the input physics. For instance, simulations with heat conduction consistently predict smoother temperature distributions, thus X-ray spectroscopic biases are minimal in this case. On the other hand, "adiabatic" simulations predict long-lasting high-density cool-core type phenomena, which will lead to significant biases in single-temperature fits. Estimates of biasing due to temperature inhomogeneities can range up to 10 or 15 percent (e.g., Rasia et al. 2012).

Finally, for HE mass estimates obtained from X-ray data, instrument calibration uncertainties also play a significant role in introducing uncertainties in mass estimates. For instance, the difference in calibration between *XMM-Newton* and *Chandra* can induce differences in Y_X. This is typically 5 percent, from a comparison of *XMM-Newton* based values published by Planck Collaboration XI (2011) to *Chandra* values for 28 ESZ clusters by Rozo et al. (2012). This can lead to differences of up to 10 percent in the mass $M_{500}^{Y_X}$ derived from Y_X, owing to the dependence of the mass on Y_X.

Thus our adopted baseline value of $(1-b) \simeq 0.8$, ranging from 0.7–1, appears to encompass our current ignorance of the exact bias.

A.5. Conclusions

In summary the baseline is

$$E^{-2/3}(z)\left[\frac{D_A^2\,Y_{500}}{10^{-4}\,\mathrm{Mpc}^2}\right] = 10^{-0.19\pm0.02}\left[\frac{(1-b)M_{500}}{6\times10^{14}M_{sol}}\right]^{1.79\pm0.08}, \quad (A.15)$$

with an intrinsic scatter of $\sigma_{\log Y} = 0.075$ and a mean bias $(1-b) = 0.80^{+0.2}_{-0.1}$. The statistical uncertainty on the normalization is about 5% and the error budget is fully dominated by the systematic uncertainties.

[1] APC, AstroParticule et Cosmologie, Université Paris Diderot, CNRS/IN2P3, CEA/lrfu, Observatoire de Paris, Sorbonne Paris Cité, 10, rue Alice Domon et Léonie Duquet, 75205 Paris Cedex 13, France
[2] Aalto University Metsähovi Radio Observatory, Metsähovintie 114, FIN-02540 Kylmälä, Finland
[3] Academy of Sciences of Tatarstan, Bauman Str., 20, Kazan, 420111, Republic of Tatarstan, Russia
[4] African Institute for Mathematical Sciences, 6-8 Melrose Road, Muizenberg, Cape Town, South Africa

[5] Agenzia Spaziale Italiana Science Data Center, c/o ESRIN, via Galileo Galilei, Frascati, Italy
[6] Agenzia Spaziale Italiana, Viale Liegi 26, Roma, Italy
[7] Astrophysics Group, Cavendish Laboratory, University of Cambridge, J J Thomson Avenue, Cambridge CB3 0HE, U.K.
[8] Astrophysics & Cosmology Research Unit, School of Mathematics, Statistics & Computer Science, University of KwaZulu-Natal, Westville Campus, Private Bag X54001, Durban 4000, South Africa
[9] Atacama Large Millimeter/submillimeter Array, ALMA Santiago Central Offices, Alonso de Cordova 3107, Vitacura, Casilla 763 0355, Santiago, Chile
[10] CITA, University of Toronto, 60 St. George St., Toronto, ON M5S 3H8, Canada
[11] CNRS, IRAP, 9 Av. colonel Roche, BP 44346, F-31028 Toulouse cedex 4, France
[12] California Institute of Technology, Pasadena, California, U.S.A.
[13] Centre for Theoretical Cosmology, DAMTP, University of Cambridge, Wilberforce Road, Cambridge CB3 0WA U.K.
[14] Centro de Astrofísica, Universidade do Porto, Rua das Estrelas, 4150-762 Porto, Portugal
[15] Centro de Estudios de Física del Cosmos de Aragón (CEFCA), Plaza San Juan, 1, planta 2, E-44001, Teruel, Spain
[16] Computational Cosmology Center, Lawrence Berkeley National Laboratory, Berkeley, California, U.S.A.
[17] Consejo Superior de Investigaciones Científicas (CSIC), Madrid, Spain
[18] DSM/Irfu/SPP, CEA-Saclay, F-91191 Gif-sur-Yvette Cedex, France
[19] DTU Space, National Space Institute, Technical University of Denmark, Elektrovej 327, DK-2800 Kgs. Lyngby, Denmark
[20] Département de Physique Théorique, Université de Genève, 24, Quai E. Ansermet,1211 Genève 4, Switzerland
[21] Departamento de Física Fundamental, Facultad de Ciencias, Universidad de Salamanca, 37008 Salamanca, Spain
[22] Departamento de Física, Universidad de Oviedo, Avda. Calvo Sotelo s/n, Oviedo, Spain
[23] Department of Astronomy and Astrophysics, University of Toronto, 50 Saint George Street, Toronto, Ontario, Canada
[24] Department of Astronomy and Geodesy, Kazan Federal University, Kremlevskaya Str., 18, Kazan, 420008, Russia
[25] Department of Astrophysics/IMAPP, Radboud University Nijmegen, P.O. Box 9010, 6500 GL Nijmegen, The Netherlands
[26] Department of Electrical Engineering and Computer Sciences, University of California, Berkeley, California, U.S.A.
[27] Department of Physics & Astronomy, University of British Columbia, 6224 Agricultural Road, Vancouver, British Columbia, Canada
[28] Department of Physics and Astronomy, Dana and David Dornsife College of Letter, Arts and Sciences, University of Southern California, Los Angeles, CA 90089, U.S.A.
[29] Department of Physics and Astronomy, University College London, London WC1E 6BT, U.K.
[30] Department of Physics and Astronomy, University of Sussex, Brighton BN1 9QH, U.K.
[31] Department of Physics, Gustaf Hällströmin katu 2a, University of Helsinki, Helsinki, Finland
[32] Department of Physics, Princeton University, Princeton, New Jersey, U.S.A.
[33] Department of Physics, University of California, Berkeley, California, U.S.A.
[34] Department of Physics, University of California, One Shields Avenue, Davis, California, U.S.A.
[35] Department of Physics, University of California, Santa Barbara, California, U.S.A.
[36] Department of Physics, University of Illinois at Urbana-Champaign, 1110 West Green Street, Urbana, Illinois, U.S.A.
[37] Dipartimento di Fisica e Astronomia G. Galilei, Università degli Studi di Padova, via Marzolo 8, 35131 Padova, Italy
[38] Dipartimento di Fisica e Scienze della Terra, Università di Ferrara, Via Saragat 1, 44122 Ferrara, Italy
[39] Dipartimento di Fisica, Università La Sapienza, P. le A. Moro 2, Roma, Italy
[40] Dipartimento di Fisica, Università degli Studi di Milano, Via Celoria, 16, Milano, Italy
[41] Dipartimento di Fisica, Università degli Studi di Trieste, via A. Valerio 2, Trieste, Italy
[42] Dipartimento di Fisica, Università di Roma Tor Vergata, Via della Ricerca Scientifica, 1, Roma, Italy
[43] Discovery Center, Niels Bohr Institute, Blegdamsvej 17, Copenhagen, Denmark
[44] Dpto. Astrofísica, Universidad de La Laguna (ULL), E-38206 La Laguna, Tenerife, Spain
[45] European Southern Observatory, ESO Vitacura, Alonso de Cordova 3107, Vitacura, Casilla 19001, Santiago, Chile
[46] European Space Agency, ESAC, Planck Science Office, Camino bajo del Castillo, s/n, Urbanización Villafranca del Castillo, Villanueva de la Cañada, Madrid, Spain
[47] European Space Agency, ESTEC, Keplerlaan 1, 2201 AZ Noordwijk, The Netherlands
[48] Finnish Centre for Astronomy with ESO (FINCA), University of Turku, Väisäläntie 20, FIN-21500, Piikkiö, Finland
[49] Haverford College Astronomy Department, 370 Lancaster Avenue, Haverford, Pennsylvania, U.S.A.
[50] Helsinki Institute of Physics, Gustaf Hällströmin katu 2, University of Helsinki, Helsinki, Finland
[51] INAF - Osservatorio Astrofisico di Catania, Via S. Sofia 78, Catania, Italy
[52] INAF - Osservatorio Astronomico di Padova, Vicolo dell'Osservatorio 5, Padova, Italy
[53] INAF - Osservatorio Astronomico di Roma, via di Frascati 33, Monte Porzio Catone, Italy
[54] INAF - Osservatorio Astronomico di Trieste, Via G.B. Tiepolo 11, Trieste, Italy
[55] INAF/IASF Bologna, Via Gobetti 101, Bologna, Italy
[56] INAF/IASF Milano, Via E. Bassini 15, Milano, Italy
[57] INFN, Sezione di Bologna, Via Irnerio 46, I-40126, Bologna, Italy
[58] INFN, Sezione di Roma 1, Università di Roma Sapienza, Piazzale Aldo Moro 2, 00185, Roma, Italy
[59] IPAG: Institut de Planétologie et d'Astrophysique de Grenoble, Université Joseph Fourier, Grenoble 1 / CNRS-INSU, UMR 5274, Grenoble, F-38041, France
[60] ISDC Data Centre for Astrophysics, University of Geneva, ch. d'Ecogia 16, Versoix, Switzerland
[61] IUCAA, Post Bag 4, Ganeshkhind, Pune University Campus, Pune 411 007, India
[62] Imperial College London, Astrophysics group, Blackett Laboratory, Prince Consort Road, London, SW7 2AZ, U.K.
[63] Infrared Processing and Analysis Center, California Institute of Technology, Pasadena, CA 91125, U.S.A.
[64] Institut Néel, CNRS, Université Joseph Fourier Grenoble I, 25 rue des Martyrs, Grenoble, France
[65] Institut Universitaire de France, 103, bd Saint-Michel, 75005, Paris, France
[66] Institut d'Astrophysique Spatiale, CNRS (UMR8617) Université Paris-Sud 11, Bâtiment 121, Orsay, France
[67] Institut d'Astrophysique de Paris, CNRS (UMR7095), 98 bis Boulevard Arago, F-75014, Paris, France
[68] Institute for Space Sciences, Bucharest-Magurale, Romania
[69] Institute of Astronomy and Astrophysics, Academia Sinica, Taipei, Taiwan
[70] Institute of Astronomy, University of Cambridge, Madingley Road, Cambridge CB3 0HA, U.K.
[71] Institute of Theoretical Astrophysics, University of Oslo, Blindern, Oslo, Norway
[72] Instituto de Astrofísica de Canarias, C/Vía Láctea s/n, La Laguna, Tenerife, Spain
[73] Instituto de Física de Cantabria (CSIC-Universidad de Cantabria), Avda. de los Castros s/n, Santander, Spain

[74] Jet Propulsion Laboratory, California Institute of Technology, 4800 Oak Grove Drive, Pasadena, California, U.S.A.
[75] Jodrell Bank Centre for Astrophysics, Alan Turing Building, School of Physics and Astronomy, The University of Manchester, Oxford Road, Manchester, M13 9PL, U.K.
[76] Kavli Institute for Cosmology Cambridge, Madingley Road, Cambridge, CB3 0HA, U.K.
[77] LAL, Université Paris-Sud, CNRS/IN2P3, Orsay, France
[78] LERMA, CNRS, Observatoire de Paris, 61 Avenue de l'Observatoire, Paris, France
[79] Laboratoire AIM, IRFU/Service d'Astrophysique - CEA/DSM - CNRS - Université Paris Diderot, Bât. 709, CEA-Saclay, F-91191 Gif-sur-Yvette Cedex, France
[80] Laboratoire Traitement et Communication de l'Information, CNRS (UMR 5141) and Télécom ParisTech, 46 rue Barrault F-75634 Paris Cedex 13, France
[81] Laboratoire de Physique Subatomique et de Cosmologie, Université Joseph Fourier Grenoble I, CNRS/IN2P3, Institut National Polytechnique de Grenoble, 53 rue des Martyrs, 38026 Grenoble cedex, France
[82] Laboratoire de Physique Théorique, Université Paris-Sud 11 & CNRS, Bâtiment 210, 91405 Orsay, France
[83] Lawrence Berkeley National Laboratory, Berkeley, California, U.S.A.
[84] Max-Planck-Institut für Astrophysik, Karl-Schwarzschild-Str. 1, 85741 Garching, Germany
[85] Max-Planck-Institut für Extraterrestrische Physik, Giessenbachstraße, 85748 Garching, Germany
[86] McGill Physics, Ernest Rutherford Physics Building, McGill University, 3600 rue University, Montréal, QC, H3A 2T8, Canada
[87] MilliLab, VTT Technical Research Centre of Finland, Tietotie 3, Espoo, Finland
[88] Moscow Institute of Physics and Technology, Dolgoprudny, Institutsky per., 9, 141700, Russia
[89] Niels Bohr Institute, Blegdamsvej 17, Copenhagen, Denmark
[90] Observational Cosmology, Mail Stop 367-17, California Institute of Technology, Pasadena, CA, 91125, U.S.A.
[91] Optical Science Laboratory, University College London, Gower Street, London, U.K.
[92] SB-ITP-LPPC, EPFL, CH-1015, Lausanne, Switzerland
[93] SISSA, Astrophysics Sector, via Bonomea 265, 34136, Trieste, Italy
[94] SUPA, Institute for Astronomy, University of Edinburgh, Royal Observatory, Blackford Hill, Edinburgh EH9 3HJ, U.K.
[95] School of Physics and Astronomy, Cardiff University, Queens Buildings, The Parade, Cardiff, CF24 3AA, U.K.
[96] School of Physics and Astronomy, University of Nottingham, Nottingham NG7 2RD, U.K.
[97] Space Research Institute (IKI), Russian Academy of Sciences, Profsoyuznaya Str, 84/32, Moscow, 117997, Russia
[98] Space Sciences Laboratory, University of California, Berkeley, California, U.S.A.
[99] Special Astrophysical Observatory, Russian Academy of Sciences, Nizhnij Arkhyz, Zelenchukskiy region, Karachai-Cherkessian Republic, 369167, Russia
[100] Stanford University, Dept of Physics, Varian Physics Bldg, 382 Via Pueblo Mall, Stanford, California, U.S.A.
[101] Sub-Department of Astrophysics, University of Oxford, Keble Road, Oxford OX1 3RH, U.K.
[102] TÜBİTAK National Observatory, Akdeniz University Campus, 07058, Antalya, Turkey
[103] Theory Division, PH-TH, CERN, CH-1211, Geneva 23, Switzerland
[104] UPMC Univ Paris 06, UMR7095, 98 bis Boulevard Arago, F-75014, Paris, France
[105] Université de Toulouse, UPS-OMP, IRAP, F-31028 Toulouse cedex 4, France
[106] University Observatory, Ludwig Maximilian University of Munich, Scheinerstrasse 1, 81679 Munich, Germany
[107] University of Granada, Departamento de Física Teórica y del Cosmos, Facultad de Ciencias, Granada, Spain
[108] University of Miami, Knight Physics Building, 1320 Campo Sano Dr., Coral Gables, Florida, U.S.A.
[109] Warsaw University Observatory, Aleje Ujazdowskie 4, 00-478 Warszawa, Poland